Master Thesis in Climate Physics

TROPOMI and WRF Comparison for Understanding South Sudan Wetland Emissions

Maria Tsivlidou
ICA-6032060

November 27, 2018

Supervisors
prof. dr. Thomas Roeckmann
dr. Sudhanshu Pandey

Institute for Marine and Atmospheric Research Utrecht (IMAU)
Utrecht University
Utrecht, The Netherlands
and
Netherlands Institute for Space Research (SRON)
Utrecht, The Netherlands

Universiteit Utrecht

SRON
Netherlands Institute for Space Research

Abstract

Methane (CH_4) is the second most important atmospheric greenhouse gas after CO_2. Due to its shorter lifetime compared to CO_2, it is a good target for short-term global warming mitigation. The recently launched instrument TROPOspheric Monitoring Instrument (TROPOMI) provides us with atmospheric total column measurements of CH_4 at an unprecedented combination of high spatial resolution of $\sim 7 \times 7\ km^2$ and daily global coverage. Consequently, TROPOMI can allow us to detect and quantify localized sources of CH_4 that can be reduced to effectively mitigate global warming. After only its first month in orbit, TROPOMI measured an unexpected high concentration of CH_4 over the South Sudan region. In this study, we examine TROPOMI data in this region for the time period of November-December 2017, and we compare it with simulations of CH_4 total column concentrations produced by the atmospheric transport model WRF-CHEM. We find that the model underestimates the CH_4 spatial gradients mainly because of too low input emissions. We find that the model concentration enhancement, due to the wetland or anthropogenic emissions, is approximately 8 times lower than the enhancement measured by TROPOMI.

Further, we analyze monthly averaged XCH4 data from TROPOMI. We find that monthly TROPOMI XCH4 enhancement follows the spatial pattern of high resolution wetland map and shows seasonality consistent with CH_4 emissions from a process-based wetland model. Thus, it is likely that the enhancement is caused largely by CH_4 emissions from wetlands. We also quantify CH_4 emissions from TROPOMI data for November and December 2017 via a measurement-only (transport model-independent) approach. Overall, we estimate that the Sudd wetlands in the South Sudan region emitted 1057 ± 447 tonnes of CH_4 per hour in November 2017 and 566 ± 348 tonnes of CH_4 per hour in December, 2017. Comparing these results with the available CH_4 emissions estimates from different process-based models, we find that the models highly underestimate the Sudd wetland emissions.

Acknowledgements

First of all, I would like to thank my thesis supervisor, Sudhanshu Pandey for his guidance and support during the completion of this thesis. Sudhanshu always found time for me, even to discuss my trivial questions and encourage me in the difficulties that I faced.

In addition, I would like to express my gratitude to Ilse Aben and Sander Houweling for the guidance, advice and discussions during this project. Also, I would like to thank the Earth science group of SRON–especially Pankaj Sadavarte–and Thomas Roeckmann, for the feedback and suggestions.

Further, I wish to thank the SRON interns for their cooperation and support during the last four months. The coffee breaks were a nice escape from work from time to time.

Last but not least, I would like to thank my friends in Utrecht that made my life in The Netherlands more pleasant and enjoyable. More importantly, I wish to express my gratitude to my family in Greece that has been supporting me all these past years and helped me to achieve my goals.

Contents

List of Figures

List of Tables

Glossary

CH_2O Formaldehyde.

CH_4 Methane.

CO Carbon Monoxide.

CO_2 Carbon Dioxide.

NETCDF Network Common Data Form.

NO_2 Nitrogen Dioxide.

O_3 Ozone.

OH Hydroxyl Radical.

RemoTeC Full physics retrieval algorithm.

S5P L2 CH4 TROPOMI data product.

SO_2 Sulphur Dioxide.

WPS WRF Preprocessing System.

WRF-CHEM Weather Research and Forecasting Model with coupled online chemistry.

XCH4 Column averaged dry air mole fraction of atmospheric methane.

XCH4_precision XCH4 precision.

XCH4_priori XCH4 priori model.

Acronyms

AOT Aerosol Optical Thickness.

ARW Advanced Research WRF core.

BG Background box.

CAMS Community Atmosphere Model.

DX Enhancement of methane.

ECMWF European Centre for Medium-Range Weather Forecasts.

EDGAR Emissions Database for Global Atmospheric Research.

EIA U.S Energy Information Administration.

EPA Environmental Protection Agency.

ESA European Space Agency.

GHG Greenhouse Gas.

GOSAT Greenhouse Gases Observing Satellite.

GWP Global Warming Potential.

HR High Resolution.

IME Integrated Mass Enhancement.

LPJ Lund-Potsdam-Jena Model.

LR Low Resolution.

NSO Netherlands Space Office.

Q Emission rate.

S-5P Sentinel-5 Precursor.

SCIAMACHY SCanning Imaging Absorption spectroMeter for Atmospheric CHartographY.

SR Source box.

SWIR Short-Wave InfraRed.

TROPOMI TROPOspheric Monitoring Instrument.

U Mean absolute wind speed of the source box.

UTC Coordinated Universal Time.

W Length of side of the source square box.

WRF Weather Research and Forecasting Model.

1 Introduction

Methane is a greenhouse gas present in the atmosphere of Earth and is a major cause of the current global warming. The recently launched TROPOspheric Monitoring Instrument (TROPOMI) provides us with high quality measurements of methane, allowing to study its sources in unprecedented detail. During its first month in operation, TROPOMI observed unexpectedly high concentrations of methane in South Sudan region.

We begin this chapter, section 1.1, describing the role of methane in global warming. Subsequently, in section 1.2 we describe TROPOMI methane measurements and, in section 1.3, the region of interest South Sudan. In section 1.4, we explain the concrete objectives of this study and we conclude, in section 1.5, explaining how the rest of the document is organized.

1.1 Methane and Significance

Methane (CH_4) is a major atmospheric Greenhouse Gas (GHG). CH_4 is the second most important GHG after CO_2 [Stocker et al., 2013]. Even though its concentration in the atmosphere is 200 times lower than CO_2, on a molecule-for-molecule basis CH_4 is more powerful than CO_2 because of its higher Global Warming Potential (GWP) [Stocker et al., 2013].

According to the Environmental Protection Agency (EPA) [EPA], GWP is defined as the amount of heat that is absorbed by emissions of 1 ton of gas over a specific period of time, relative to the emissions of 1 ton of CO_2. As a result, the reference GWP of CO_2 is by default equal to 1 regardless the time horizon that is examined. On the other hand, the GWP of CH_4 is equal to 84 computed over a 20-year period [Stocker et al., 2013]. The GWP index of CH_4 is computed taking into account also its indirect effects. For instance, CH_4 is a precursor of ozone (O_3) which is itself a greenhouse gas [Stocker et al., 2013](IPCC, 2001). Hence, the global warming impact of CH_4 is very important. Further, CH_4 has a short lifetime of approximately 12.4 years [Stocker et al., 2013] in contrast with CO_2 whose lifetime varies from 30 to 95 years [Jacobson]. Consequently, a reduction in CH_4 concentration can lead to rapid positive effects on atmospheric

warming. Overall, due to its short lifetime and its large GWP, CH_4 is considered a good target for short term climate change mitigation.

1.1.1 Methane Budget

There are several sinks responsible for the removal of CH_4 from the atmosphere. The dominant sink is the reaction with hydroxyl radical (OH), mainly in the troposphere, which contributes 90% of the total loss. The oxidation of CH_4 by OH produces water and CO_2. The second most important sink is its transport to stratosphere, where CH_4 is also oxidised. Another sink with a minor significance is the destruction of CH_4 by bacteria (methanotrophs) found in soil, which consume CH_4 as a source of carbon and energy [Jacob, 1999, Saunois et al., 2016].

According to Ciais et al. [2014], from pre-industrial times to up until 2015, the concentration of CH_4 in the atmosphere has nearly tripled from 700 to 1834 parts per billion (ppb). Despite its large growth and significant role in climate change, and even though its total global emissions and atmospheric sinks are relatively well known, CH_4's budget is not fully understood yet [Prather et al., 2012, Saunois et al., 2016].

The global emission of CH_4, as calculated by Saunois et al. [2016], is approximately $558[540\text{-}568]\ Tg$ per year. However, our estimations as regards each individual source of CH_4 are extremely uncertain; our knowledge about each individual contribution is not adequate yet [Stocker et al., 2013, Dlugokencky et al., 2011, Houweling et al., 2014].

CH_4 is emitted in the atmosphere by sources of both natural and anthropogenic origin. Anthropogenic processes play important role in CH_4 budget as approximately 60% of CH_4 is produced by human activities [Saunois et al., 2016]. The most important anthropogenic sources are agricultural and waste processes (see table 1.1 and fig. 1.1). Some representative instances of such sources are landfills and rice cultivations that, under anaerobic conditions (oxygen-free), emit CH_4. Also, livestock production (mainly through enteric fermentation in animals) including animal manure produce CH_4. Another important source is the fossil fuel sector that includes coal mining and oil and gas industry where industrial processes such as production, processing, transfer and storage release CH_4. Another anthropogenic source with minor significance is biomass and biofuel burning, which release CH4 due to incomplete combustion as a side product.

Under the natural sources category, the most dominant source are natural wetlands where anaerobic decomposition of organic carbon occurs. The rest of the natural sources, for example, termites, wild animals, wildfires, and geological sources, have a minor contribution to CH_4 emissions.

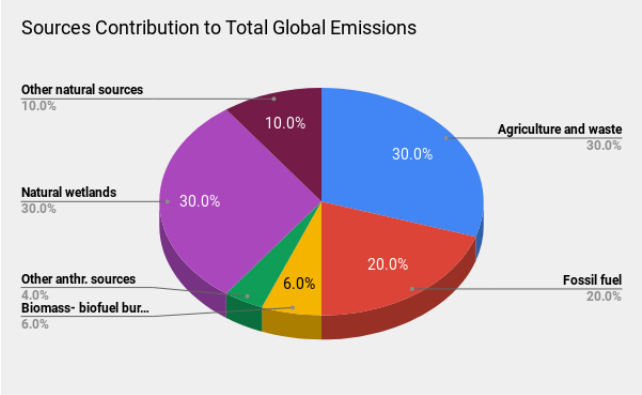

Figure 1.1: The pie chart shows the approximate contribution of each source to the total global emissions [Saunois et al., 2016]. Detailed reviews of CH_4 global budget can be also found in Saunois et al. [2016].

1.2 TROPOMI

Sentinel-5 Precursor (S-5P) satellite [Veefkind et al., 2012] is an atmospheric chemistry mission that was launched on 13 October 2017. An illustrative diagram of the S-5P instrument is shown in fig. 1.2. The primary target of S-5P is to provide atmospheric tracer measurements from space for the domain of air quality and climate change. The TROPOspheric Monitoring Instrument (TROPOMI) is the only instrument onboard the S-5P satellite, which developed with a collaboration between European Space Agency (ESA) and Netherlands Space Office (NSO).

Figure 1.2: Illustration of Sentinel-5 Precursor satellite with one single payload on board, TROPOMI (Source: ESA/ATG medialab).

Table 1.1: The Table presents global CH_4 emissions of each source category in Tg CH_4 per $year$. The ranges indicate the 1-σ uncertainties. Please note that differences of $1Tg$ CH_4 yr^{-1} in the totals can occur because of rounding errors. Detailed reviews of CH_4 global budget can be also found in Saunois et al. [2016]

.

Time Period	**2003-2012**	
	Tg/yr	Uncertainty Range
NATURAL SOURCES	231	[194-296]
Natural Wetlands	167	[127-202]
Other natural sources	64	[21-132]
ANTROPOGENIC SOURCES	328	[259-370]
Agriculture and waste	188	[115-243]
Fossil fuels	105	[77-133]
Biomass and biofuel burning	34	[15-53]
SINKS	548	
Total Chemical loss	515	
Soil uptake	33	[28-38]
SUM OF SOURCES	558	[540-568]
SUM OF SINKS	548	
IMBALANCE	10	
ATMOSPHERIC GROWTH	10	[9.4-10.6]

TROPOMI is flying in a sun-synchronous orbit at altitude of 824 km with local overpass time 13:30 pm. It is a multispectral imaging spectrometer that detects solar radiation reflected or scattered back to space from Earth's atmosphere and surface. As the spectral fingerprint of each target atmospheric trace gas is known, its concentration can be calculated from the measured spectra and information about path length of the light (see fig. 1.3). The retrieval algorithm calculates the total column concentration for the trace gas by iteratively fitting spectral observation of backscattered light to a modeled spectrum.

Compared to its heritage instruments, TROPOMI has a wide range of advantages since it combines the best features of each and in most cases it improves their performance (see fig. 1.4). For instance, it has the comparable (or better) resolution than GOSAT ($10 \times 10 km^2$). GOSAT has fairly low spatial sampling. SCIAMACHY, on the other hand, has good spatial sampling but low precision and large pixel size.

Further, TROPOMI has an improved signal-to-noise ratio ($2-5\%$) for measurements under low albedo conditions. TROPOMI has a very high spatial resolution (3.5×7 km^2 for all trace gases, except for CO and CH_4 that is $7 \times 7 km^2$). As a result, for the first time it is possible to detect air pollution on

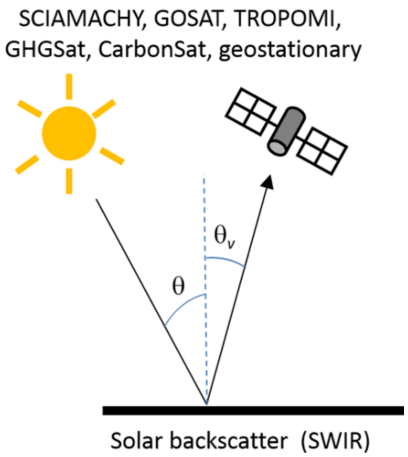

Figure 1.3: Illustration for measuring CH_4 from space. θ is the solar zenith angle and θ_v is the satellite viewing angle (Source: Jacob et al. [2016]).

facility and city scale from space [Borsdorff et al.]. With such fine resolution, it can distinguish individual sources of pollution and provide us with more dense measurements [Borsdorff et al., 2018].

TROPOMI has more spectral bands than its predecessors: ultraviolet and visible (270-500 nm), near-infrared (675-77 nm), and shortwave infrared (2305-2385 nm). This allows TROPOMI to measure a wider range of atmospheric trace gases such as nitrogen dioxide (NO_2), ozone (O_3), formaldehyde (CH_2O), sulphur dioxide (SO_2), methane (CH_4), and carbon monoxide (CO). In addition, it observes clouds and aerosols-related parameters, which can be fed into the retrieval algorithms of trace gases.

Furthermore, TROPOMI follows a polar sun synchronous orbit to scan a stripe of the Earth using a two dimensional detector (See fig. 1.5). The dimension of the strip across the track of the satellite, the so called swath, is $2600\,km$, while along the track is $7\,km$. TROPOMI takes a measurement every 1 second. The detector is a two dimensions array of sensors: one dimensions is used to measure spatial information and the other to measure spectral information. Hence, for every ground pixel, a large spectral range is measured and TROPOMI can measure more tracers than the previously launched satellite. Completing 14-15 orbits per day, TROPOMI accomplishes global coverage on a daily basis [Veefkind et al., 2012, Nijkerk et al., 2012](see fig. 1.6).

Emission inventories are category-wise, spatiotemporal records of emissions of atmospheric trace gases. Using these datasets as input, an atmospheric transport models simulates the concentration of the trace gas in space and time. Using these datasets air quality can be monitored and policies to mitigate the pollution can be implemented. However, the emission inventories are often inadequate due to ,for instance, lack of continuity in the data they rely on,

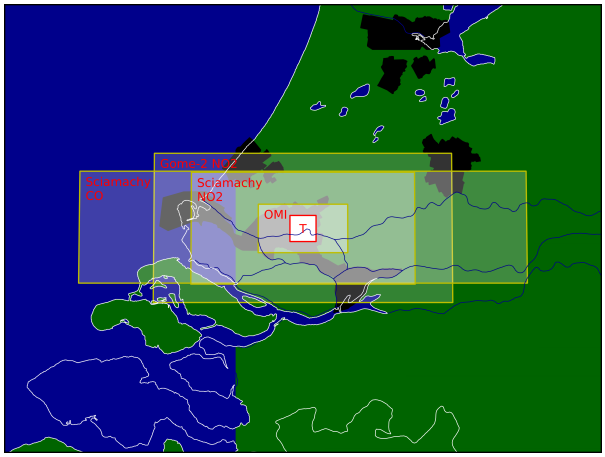

Figure 1.4: Illustration of TROPOMI pixel size (nadir pixel) in comparison with previous and current satellites.

Source: `http://www.tropomi.eu/gallery/science-data-products-gallery`

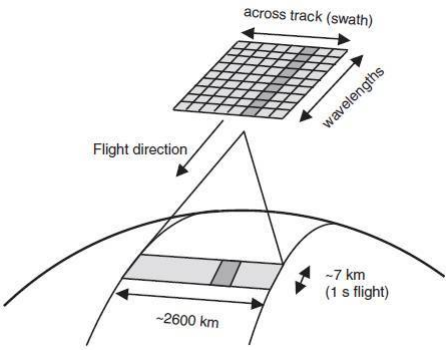

Figure 1.5: TROPOMI measurement principle (Source: Nijkerk et al. [2012]).

incapability to account for extreme weather events and random event such as volcanic eruptions ([ESA]).

An efficient way to calibrate the inventories is to use the information of satellite measurements. TROPOMI is capable of detecting variability of the trace gas sources and provide detailed information about their spatio-temporal evolution [van Weele et al., 2008]. With its high spatial resolution, it can map sources even on a city scale. The quantification of individual anthropogenic and natural sources and the validation of inventories using the TROPOMI measurements can lead to a significant reduction in uncertainties of the trace gas inventories. Using the novel TROPOMI data, a major improvement of the emission inventories is expected.

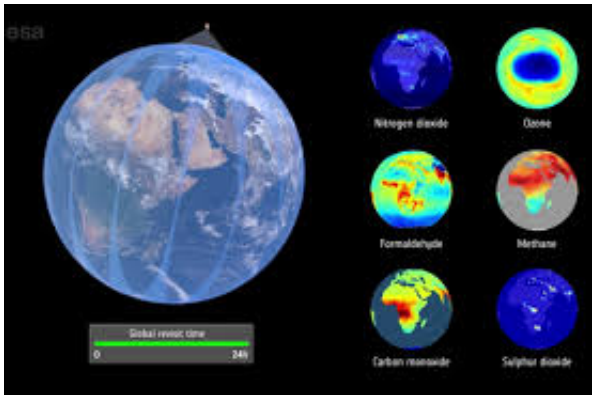

Figure 1.6: Illustration of TROPOMI global coverage and examples of atmospheric trace gases that it can measure.

Source: `http://www.tropomi.eu/gallery/tropomi-daily-coverage`

1.3 Study Area: South Sudan

South Sudan, officially known as Republic of South Sudan, is the world's newest country since it gained its independence from Sudan on 2011 after decades of civil war. It is located in the North Eastern Africa, between 3° and 13°N latitudes, and 24° and 36°E longitudes (see fig. 1.7).

Figure 1.7: Location of South Sudan.

Frankenberg et al. [2011] , identified South Sudan as a significant localized CH_4 source. This result was inferred by averaging seven years of CH_4 observations of SCIAMACHY. On the other hand, Hu et al. [2018] observed an enhancement of CH_4 over South Sudan after averaging only first one month of TROPOMI measurements (see fig. 1.8). The spatial structure of the CH_4 enhancement follows the structure of the biggest wetland expanse of South Sudan, Sudd.

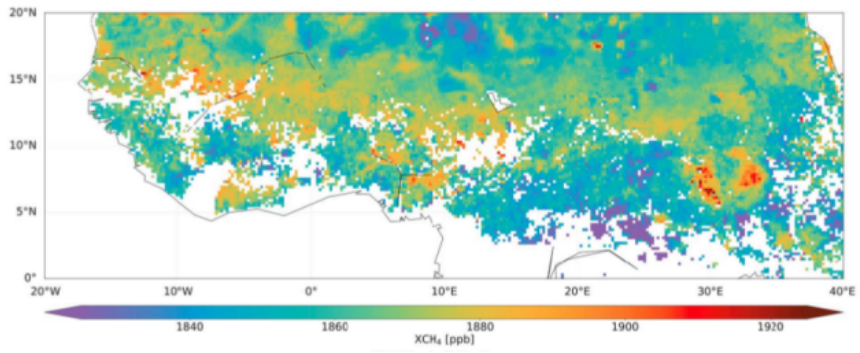

Figure 1.8: CH_4 mixing ratio retrieved by TROPOMI over western and central Africa, averaged for the time period between 12 November and 30 December 2017 (Source: Hu et al. [2018]).

However, the data from a processes-based bottom-up model for wetland emissions (LPJ model, see section 2.2.2), suggests that Sudd is not one of the most important wetland regions worldwide. Figure 1.9 compares the CH_4 emission of LPJ over the region of South Sudan and *Paraguay*. Globally the Sudd wetlands have the 10th position in the rankings of wetland with highest CH_4 emissions (see fig. 1.9).

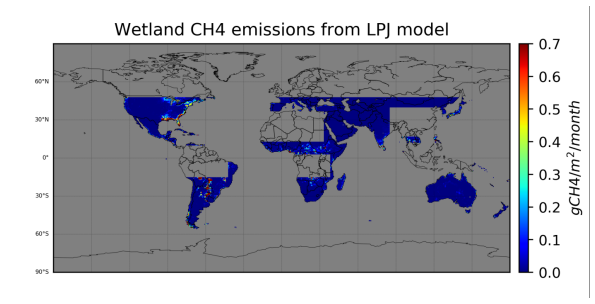

(a)

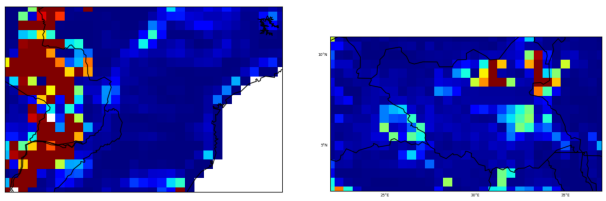

(b) (c)

Figure 1.9: a) Illustration of averaged CH_4 emissions from LPJ wetland model for the months of November-December adapted to the area where TROPOMI has signal, LPJ emissions focused over the regions of b) Paraguay and c) South Sudan.

Another cause of the South Sudan CH_4 enhancement can be anthropogenic CH_4 emissions. According to U.S Energy Information Administration (EIA), most of South Sudanese oil producing assets are located near or across the shared borders between Sudan and South Sudan, not very far from where the CH_4 enhancement is observed (see fig. 1.10). Overall, the cause of CH_4 enhancement over South Sudan as measured by TROPOMI needs a better explanation.

(a)

Source: `http://news.bbc.co.uk/nol/shared/spl/hi/world/10/sudan/img/sud_oil.gif`

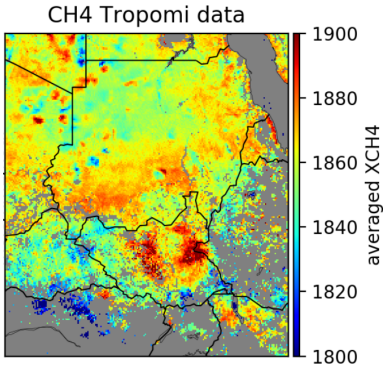

(b)

Figure 1.10: a) Oil and Gas oil producing assets located near or across the shared borders between Sudan and South Sudan. b) Averaged CH_4 mixing ratio retrieved by TROPOMI for the time period between 12 November and 30 December 2017. It is observed that the general patterns of CH_4 enhancements and oil assets show some similarity in the structure, however, the latter are shifted southeastward.

1.4 Objectives

After the launch of TROPOMI, exciting results are expected in the fields of atmospheric composition and air quality. Using the high quality measurements of TROPOMI, we investigate the CH_4 sources over South Sudan in details. Specifically, we qualify and quantify CH_4 emissions over the region of South Sudan. The primary purpose is to find out the dominant sources that are responsible for the CH_4 enhancement observed in TROPOMI data. This is done via the following steps:

- We use the Atmospheric Transport Model, WRF, to convert the CH_4 emissions from wetland model and inventories into atmospheric concentration. Moreover, we compare it with the CH_4 mixing ratio retrieved by TROPOMI for the months of November and December 2017.
- We verify the accuracy of existing emission inventories by comparing them with the emissions calculated from TROPOMI data using a transport model-independent method called the Source Pixel method.

1.5 Organization

The rest of this master thesis is divided in 3 chapters:

In chapter 2, we give the reader a brief explanation of the analysis method used for this study. We describe the orbital and the monthly averaged TROPOMI data. We present the atmospheric transport model used to simulate the CH_4 concentration over the region of South Sudan and explain the method used to quantify of emission rates of CH_4.

In chapter 3, we present the results of this master thesis. We compare the model with observations from TROPOMI in order to find out whether the model and the agree. Moreover, we quantify CH4 emission from TROPOMI data and compare this result to several bottom-up wetland models of CH_4 emission.

We conclude this document, in chapter 4, with a few remarks about this study and a discussion about the results. We also indicate possible further directions of research on the subject.

2 Data and Methods

In this chapter, we explain the data and methods used in our analysis. We start in section 2.1 by introducing the TROPOMI CH_4 product. We continue, in section 2.2, with a brief description of the Atmospheric Transport Model used to simulate the atmospheric CH_4 concentration and their comparison with the observations. Finally in section 2.3, we introduce a model-independent emission quantification approach, the Source Pixel method, and process-based wetlands models of CH_4 emissions.

2.1 TROPOMI Data Product

2.1.1 Retrieval Approach

As mentioned in section 1.2, TROPOMI operates in several spectral bands measuring solar backscattered radiation. For this study, we use only spectral measurements from the short-wave infrared (SWIR) band as we focus on CH_4 that absorbs radiation at $2.3\ \mu m$. The column-averaged dry air mole fraction of atmospheric CH_4 (XCH4) is calculated with near uniform sensitivity in the troposphere taking into consideration CH_4's absorption features [Jacob et al., 2016, Hu et al., 2018].

Aerosols and cirrus particles present in the atmosphere modify the lightpath of the measured solar backscattered radiation. For instance, the lightpath is shortened when it is reflected back to space without penetrating the whole atmospheric column (see fig. 2.1). This would lead to an underestimation in the XCH4 in comparison to the real or true XCH4 (see middle panel of fig. 2.1). Higher surface albedo, on the other hand, can increase the length of the lightpath in presence of aerosol and cirrus leading to an overestimate of XCH4 (see right panel of fig. 2.1). Consequently, not taking into account possible lightpath changes can induce substantial biases in the measured XCH4.

In order to reduce the error due to modified lightpath, the computation of XCH4 is done using the full physics retrieval algorithm, RemoTeC [Butz et al., 2009, 2011, Hasekamp and Butz, 2008, Hu et al., 2016]. This algorithm

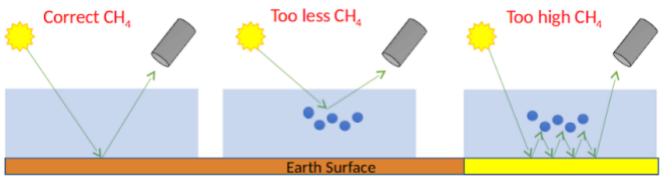

Figure 2.1: Illustration of the scattering of light by aerosol and cirrus particles in the atmosphere. The left panel shows an idealized case without scattering. The middle and right panels show the shortening and increase of the light path due to scattering resulting in an underestimation and overestimation of CH_4 mixing ratio, respectively.

retrieves scattering properties such as amount, size and height of aerosols and surface albedo, simultaneously with the CH_4 column, to account for the light path modification.

2.1.2 TROPOMI XCH4

Herein, we use S5P L2 CH4 data product that includes XCH4 measurements retrieved from TROPOMI. In the version of the data that we use (10.9, one band retrievals), an additional more strict filtering is applied to minimize the error caused by cirrus [Hu et al., 2018].

The data for each TROPOMI orbit is a NETCDF format file. For this analysis, we use only the orbits where TROPOMI has signal over the region of interest (between 2° and 11.5° N latitudes and 24° and 36° E longitudes), for the months of November and December 2017. We set a threshold of 100 pixels of valid measurements per orbit to exclude orbits with sparse coverage. Table 2.1 shows the adequate orbits for both months. The specific variables taken from the dataset for our study are displayed in table 2.2.

Table 2.1: Orbits with adequate TROPOMI data for the months of November and December 2017 after applying threshold of 100 valid measurement per orbit for the region between 2° and 11.5° N latitudes and 24° and 36° E longitudes)

November		**December**	
Orbit	Data	Orbit	Date
568	22-11-2017	923	19-12-2017
625	26-11-2017	937	18-12-2017
639	27-11-2017	1079	28-12-2017
		1093	29-12-2017

Table 2.2: Variables from the S5P L2 CH4 product data used in the study. Nobs is number of observations.

Name	Units	Dimension	Description
time	sec	nobs	Time of measurement (seconds since 1970-01-01 00:00:00)
latitude_center	Degrees North	nobs	Center latitude of measurement
longitude_center	Degrees East	nobs	Center longitude of measurement
lat_corners	Degrees North	(nobs, 4)	Corner latitude of measurement
lon_corners	Degrees East	(nobs, 4)	Corner longitude of measurement
XCH4	ppb	nobs	Column averaged dry air mixing ratio of CH_4
XCH4_precision	ppb	nobs	Precision of XCH4
XCH4_priori	ppb	nobs	A priori value of column averaged dry air mixing ratio of CH_4
surface_pressure	hPa	nobs	Surface pressure
aerosol_optical_thickness	dimensionless	nobs	Aerosol optical thickness
surface_albedo	dimensionless	nobs	Surface albedo
u10	m/sec	nobs	Eastward wind component at $10\,m$ height
v10	m/sec	nobs	Northward wind component at $10\,m$ height
qa_value	dimensionless	nobs	Value for filtering: 0.4: pre-filter but not post-filter 1: post-filtered data (strict filter)

2.1.3 Re-gridding of TROPOMI data

For further analysis of TROPOMI data, we produce a map of monthly averaged XCH4 on a regular grid with spatial resolution of 0.1×0.1 degrees. Every orbit that TROPOMI measures has a different spatial distribution of grid cells, depending on the viewing zenith angle at the moment of the observation. For this reason, we do regridding for each day of November and December, taking into account all the available orbits for the region of interest. Afterwards, we combine all the regridded orbital sets to calculate separately the monthly mean of XCH4 for each month.

To improve the accuracy of the data, we compute the orbital regridding of XCH4 weighting the value of each TROPOMI pixel with its XCH4_precision. Hence, each pixel contributes to the final mean XCH4 of the grid cell according to its precision: the more precise a pixel is, the more it contributes. The advantage of computing precision weighted averaged data is that we decrease the influence of the data points with worse precision.

For each grid cell of 0.1×0.1 degrees, the regridded average XCH4, $XCH4_{avg}$,

is computed as follows: For each orbital file, there are several measurements (TROPOMI pixels) of XCH4 and XCH4_precision in *each grid cell*:

$$XCH4_{avg} = \frac{\sum x * p^{-2}}{\sum p^{-2}} \tag{2.1}$$

where x is XCH4 and p is XCH4_precision of a TROPOMI pixel measurement.

The XCH4 precision error, σ_{pr} for each grid cell is computed as:

$$\sigma_{pe} = \frac{1}{\sqrt{\sum p^{-2}}} \tag{2.2}$$

For other variables such as surface pressure, surface albedo, aerosol column, etc. (see table 2.2), we use the arithmetic mean to calculate the monthly average of the regridded data. As opposed to the calculation of XCH4, the error for these variables is assumed negligible.

2.2 Atmospheric Transport model

2.2.1 WRF model

In this study we use the Weather Research and Forecasting (WRF) Model version 3.7, with the Advanced Research WRF core (ARW) [Skamarock et al., 2008]. It is a non-hydrostatic numerical model capable of creating simulation of atmospheric tracers. To account for variabilities caused by atmospheric transport in our simulation, we use a built-in CHEM module of WRF model, [Grell et al., 2005].

The first step to run the model is to set the input of the transport simulation by running WRF Preprocessing System (WPS). This system contains three programs: *geogrid, ungrib and metgrid* that are used for initializing the topographical and meteorological conditions (fig. 2.2).

The output of WPS has to be adjusted with realistic conditions. To do so, the program *real* defines the initial and boundary CH_4 concentration conditions based on the CAMS model dataset. The initial conditions provide the model with information about the time initial concentration of CH_4 in the target region. The boundary conditions represent the spatial initial concentration of CH_4 transferred to the model domain from spatial boundaries.

At this point, CH_4 emissions have to be taken into consideration (see section 2.2.2). Sinks of CH_4 are disregarded because they are negligible for the model run time period compared to the lifetime of CH_4 in the atmosphere (see section 1.1). After the previous steps, the main transport model, *wrf*, can be executed as shown in fig. 2.2.

For our study, we run the model for the domain between 2° and 11.5° N latitudes and 24° and 36° E longitudes. The spatial resolution is $7 \times 7\,km^2$ and

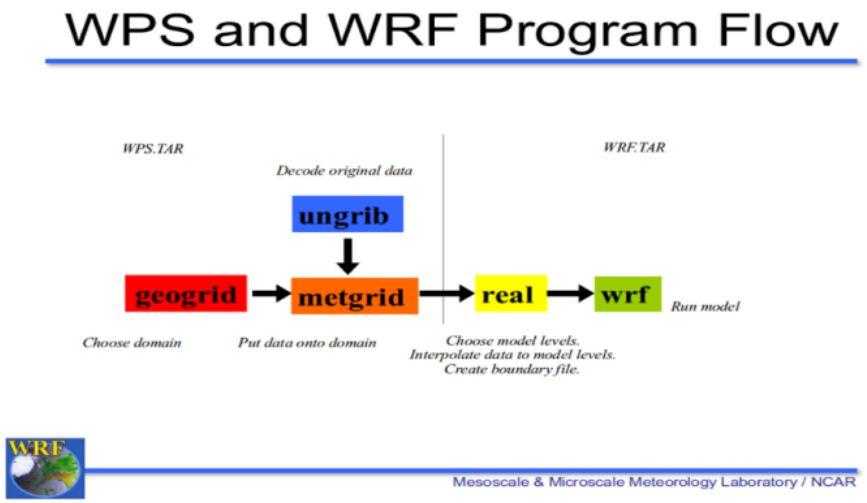

Figure 2.2: Program flow of WRF. Under WPS module: *geogrid* calculates the topographic information for the focus region, *ungrid* decodes meteorological data from GRIB-format files and *metgrid* spatially interpolates this meteorological data for the region. Under WRF module, *real* creates, initial and boundary conditions for the simulation. Finally, WRF is executed to run the transport model with CH_4 emissions from different sources as input.

Source: `http://www2.mmm.ucar.edu/wrf/users/tutorial/tutorial_presentation_summer_2015.htm`

the time comprehends between 1 of November and 20 December with a time resolution of 60 seconds.

2.2.2 Emission Dataset

Using the WRF model we simulate CH_4 concentrations over the region of South Sudan, taking into consideration CH_4 emissions from several sources: anthropogenic inventories, wetland model and point oil and gas sources.

The WRF model is based on grid equidistant in km. On the other hand, the grid of emission inventories is in degrees. Therefore, we interpolate the inventories to the WRF grid. In addition, WRF emission unit is $moles/km^2/hour$ but each inventory uses its own units of measure.

Anthropogenic. For the anthropogenic emissions we use Emissions Database for Global Atmospheric Research (EDGAR) v4.3.2 inventory with spatial resolution of 0.1 degrees (See fig. 2.3). This dataset contains the annual mean emissions of CH_4 for the year 2012 measured in $kg/m^2/sec$ [Crippa et al., 2018].

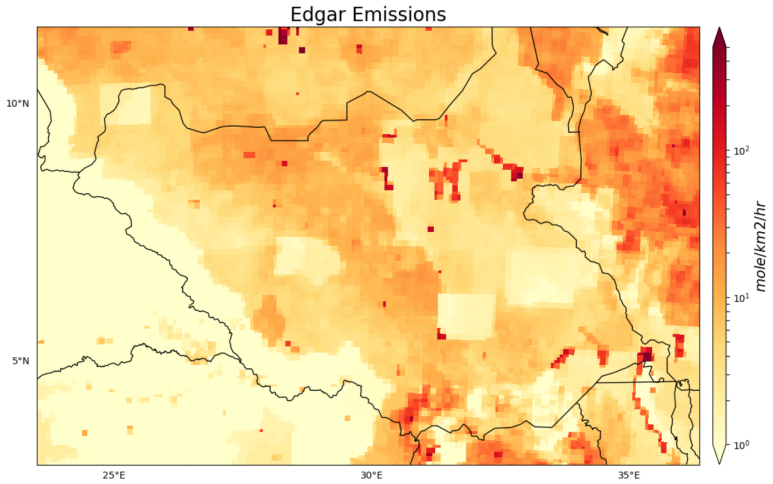

Figure 2.3: EDGAR emissions interpolated to the WRF emission grid.

Wetland. We use CH_4 data from LPJ process-based model that represents the wetland emissions [Hodson et al., 2011]. The LPJ dataset has a spatial resolution 0.5 degrees and consists of the monthly mean CH_4 emissions for the time period 1980-2014. For our analysis, we use the months of November and December 2014, filling the missing values of the dataset by applying a linear interpolation. LPJ also has wetland fraction for each grid cell available that expresses the inundation fraction, or the water-submerged fraction of land surface, in the grid cell.

High resolution wetland CH_4. The LPJ dataset has a coarse spatial resolution. In order to improve the resolution, we derive wetland emissions at higher spatial resolution combining a high resolution (HR) wetland fraction dataset with LPJ's CH_4 emission and its low resolution (LR) wetland fractions. The data for the HR wetland fraction is taken from the Tropical and Subtropical Wetlands Distribution version 2 dataset [Gumbricht et al., 2018]. This dataset contains information about the annual mean of wetland fraction with 231 meters spatial resolution. Wetland fraction shows a strong correlation with the CH_4 emissions (see fig. 2.4, (a)). Therefore, to compute the HR wetland emissions we use the ratio of the wetland fractions from HR and LR data as a scaling factor.

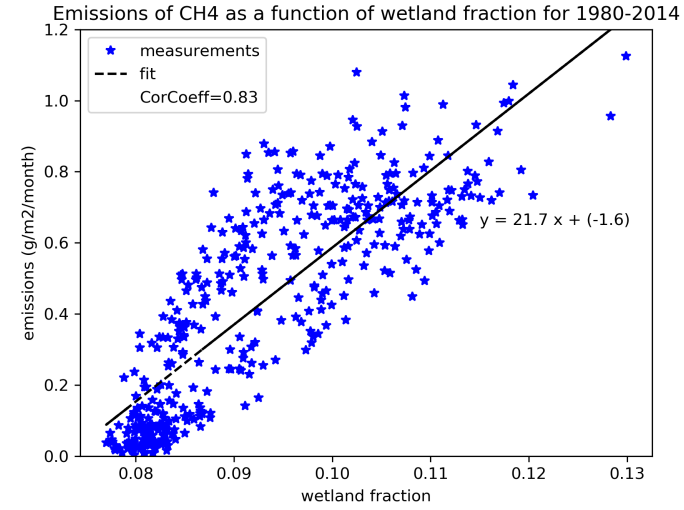

(a)

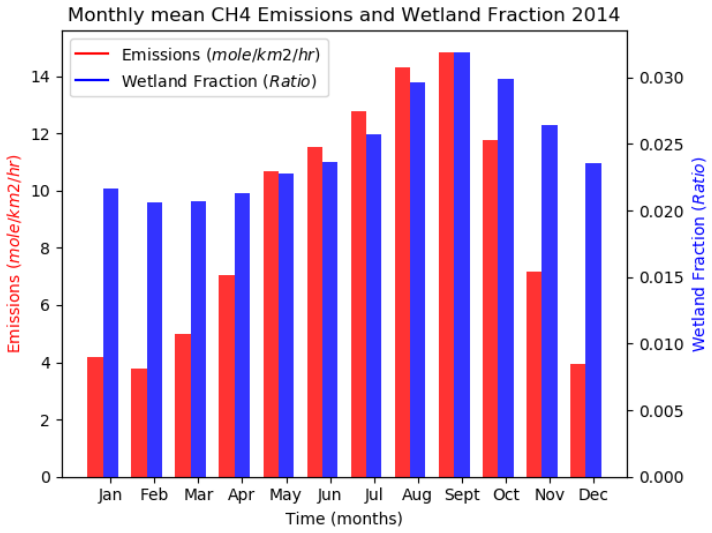

(b)

Figure 2.4: a) Monthly mean LPJ wetland emissions as a function of LPJ wetland fraction for the time period 1980 until 2014. b) Monthly mean LPJ wetland emissions (red bar, left x-axis) and wetland fraction (blue bar, right x-axis) for the year 2014. Both graphs show LPJ data for the target region.

We calculate the HR wetland emissions using the following equations:

$$w_{m,\text{HR}} = \frac{w_{m,\text{LR}}}{w_{a,\text{LR}}} * w_{a,\text{HR}} \tag{2.3}$$

$$e_{m,\text{HR}} = \frac{e_{m,\text{LR}}}{w_{m,\text{LR}}} * w_{m,\text{HR}} \tag{2.4}$$

where w: wetland fraction; e: wetland emissions; m: monthly mean; a: annual mean.

Because the wetland fraction from the HR data is annual ($w_{m,HR}$), we adjust it to the specific month by multiplying it with the wetland fraction ratio in LR ($\frac{w_{m,LR}}{w_{a,LR}}$). The emission in high resolution is then calculated as the product of the LR emission per unit of wetland fraction and the monthly wetland fraction in HR.

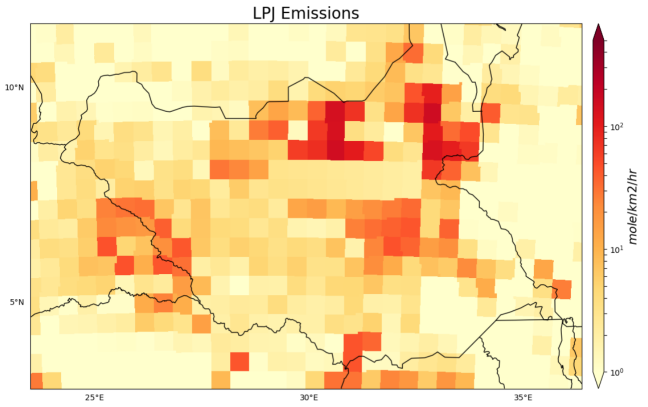

(a)

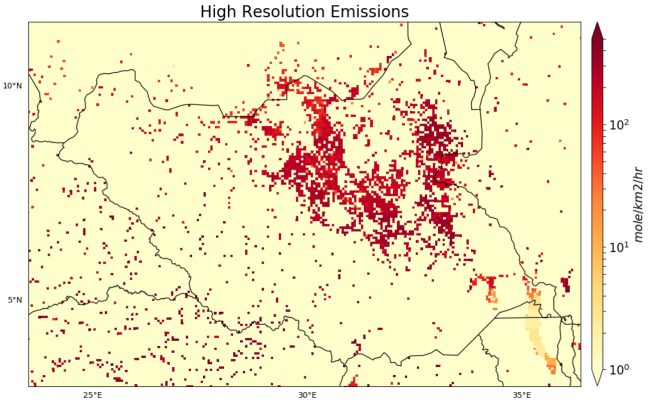

(b)

Figure 2.5: a) LPJ emissions and b) high resolution emissions interpolated to the WRF emission grid.

Oil and gas tracers. In order to get a more realistic representation of anthropogenic CH_4 emissions, we have to take into account the gas and oil activity

in the region. After executing the model only with anthropogenic and wetland emissions, we observe that the concentration is largely underestimated.

Assuming there is a missing source in our approach, we include three point sources representing the CH_4 release because of oil and gas production. Due to the current socioeconomic situation in South Sudan, there is a lack of data of GHG emissions from the region. Thus, to simulate oil and gas production, we place three point sources that emit 200 kilotonnes per year each, in the area where available maps indicate oil and gas are produced (see fig. 2.6).

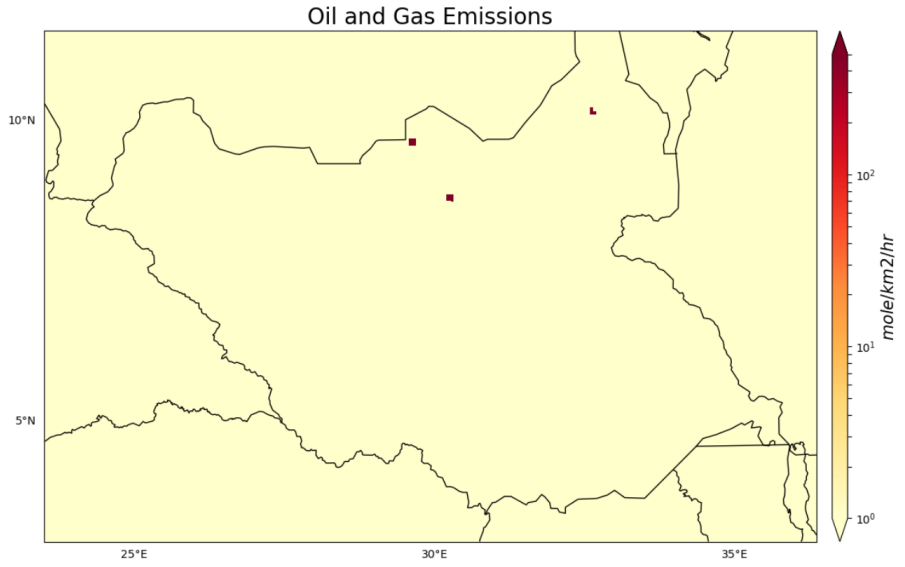

Figure 2.6: Oil and gas emissions interpolated to the WRF emission grid ($7 \times 7\ km^2$). The emissions are represented by three pixel sources located in the northern part of South Sudan.

Each oil and gas source of CH_4 is input as a separate emission tracer in the model. In the output of the model, the concentration influence of each tracer is obtained separately. To compute the total concentration of CH_4, we combine the contribution of each tracer. This can be done because WRF is an approximately linear model, which means that the concentration of CH_4 depends linearly on the emissions and boundary conditions.

2.2.3 Total Column Concentration

The WRF model calculates the concentrations of CH_4 for the input emissions. The model provides us with of CH_4 concentration at 29 layers of atmospheric pressure for every hour. TROPOMI data consists of the total column averaged concentration measurements of CH_4 the local overpass time over South Sudan (13:00 local time or 10:00 UTC).

Consequently, we need to adapt the model concentration output to TROPOMI measurements to be able to compare them. To do so, we compute the mean column concentration of CH_4 from WRF output at (10:00 UTC) using the following procedure:

In order to compute the CH_4 total column average concentration, $CH4_c$, we have to take into account the pressure gradient. We use the following equation:

$$CH4_c = \frac{(m_1 * (P_s - P_{1,b}) + m_2 * (P_{1,b} - P_{2,b}) + \cdots + m_n * (P_{n-1,b} - P_{n,b}))}{(P_s - P_{n,b})} \tag{2.5}$$

where n: layer number in the column; m: CH_4 mixing ratio in the layer; P_s: surface pressure; $P_{n,b}$: boundary pressure of the layer.

For each layer i, we multiply the CH_4 mixing ratio m_i with the pressure difference along the layer $P_{i-1} - P_i$.

However, the model does not provide directly the pressure at the boundary of each layer, but only at the center of the layer. To calculate the boundary pressure, we apply the following equation:

$$P_0 = P_s \tag{2.6}$$

$$P_{i+1} = 2 * P_{i,c} - P_i \tag{2.7}$$

where i: layer number in the column; P_s: surface pressure; $P_{i,c}$: center pressure of the layer.

2.3 Emission Quantification

To quantify individual CH_4 emissions we use multiple approaches: WRF emissions optimization, Source Pixel method, and direct assessment of emissions.

2.3.1 Optimization of WRF model emissions

In order to improve the emission estimates, we apply an optimization approach. To do so, we spatially interpolate WRF CH_4 concentrations to the TROPOMI grid and remove the data points where TROPOMI did not have measurements due to, for example, cloud cover. We define a cost function (J), for the optimization scheme, as the difference between observations and the model. In J, the WRF output of each tracer is scaled separately to understand how each one contributes independently to the total output. The difference of TROPOMI (XCH4) and the combination of the WRF tracers is the target of the optimization. We define the cost function J as follows:

$$J = \overline{\sqrt{(XCH4 - (\alpha * Boundary + \beta * Wetlands + \gamma * EDGAR \ldots))^2}} \tag{2.8}$$

The optimization of the cost function gives the scaling factors $(\alpha, \beta, \gamma, \dots)$ for each emissions tracer category of WRF. Because the tracer transport in the WRF model is linear, the contribution of each tracer to the concentration scales linearly with the emissions. Therefore, the factor multiplying a concrete tracer can be used as the scaling factor of that emission inventory.

2.3.2 Source Pixel method

The Source Pixel method [Jacob et al., 2016, Buchwitz et al., 2017] quantifies emissions using atmospheric XCH4 measurements by comparing XCH4 of possible sources region with an appropriate background region. To apply the method, first we define a square box (SR) that includes the enhancement caused by the individual source that we would like to estimate.

Then, we define a background box (BG) that has the reference value of XCH4. The location of the BG is *ideally* upwind, right before the source box and does not contain any significant emission source. Figure 2.7 illustrates a selection of SR that contains the source and BG that provides the reference value.

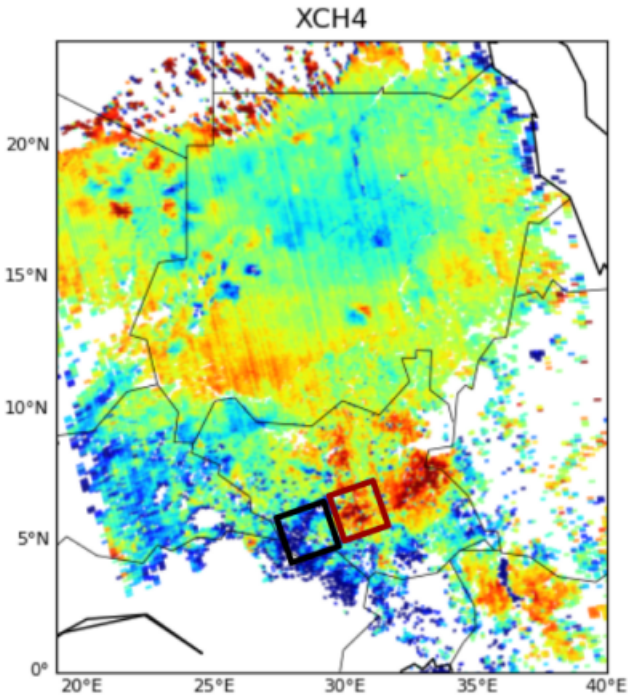

Figure 2.7: Illustration for selecting the source (red) and background (**black**) boxes.

Ideally, one would chose the BG and SR boxes in a location where the wind direction is uniform to make sure that the air passing from BG box is transferred

to the SR box without being affected by another source or being dispersed. However, the choice of the BG box might change for different applications depending on, for example, the measurement data availability.

According to Source Pixel method, the emission rate (Q) is given by the equation:

$$Q = \frac{M_{CH4}}{M_{air}} \frac{DX\ U\ p\ W}{g} \tag{2.9}$$

where M_{CH4}: molecular mass of CH_4; M_{air}: molecular mass of dry air; Q: source rate in tonnes per hour; DX: CH_4 enhancement in ppb; U: mean absolute wind speed of the source box in km per hour; W: length of side of the source square box in km; p: surface pressure; g: gravitational acceleration.

To apply the Source Pixel method to the TROPOMI data, we use the precision weighted mean XCH4 to compute the mean concentration of the source and background boxes. As a sensitivity test, we also use the median XCH4 for the calculation, instead of the mean, but the difference is negligible.

Error Calculation

In the use the Source Pixel method, we need to account for the possible errors.

In the eq. (2.9) errors in the enhancement DX directly induce an error in Q. Thus, any DX error should be taken into account in the quantification of the source. The potential error sources of Q are the following:

- **Precision error**: We quantify the accuracy of the mean XCH4 in the source and background boxes since the error contrasts its standard deviation from its mean. We use the XCH4 precision error of each TROPOMI measurement, as explained in section 2.1.3, to compute the mean error for the source and background boxes XCH4.

- **Aerosol and Surface Albedo error**: Aerosols present in the atmosphere and differences in surface albedo are other sources of errors in XCH4 measurement as we explained in section 2.1.1. These properties may shorten or enlarge the lightpath leading to an underestimation or overestimation of XCH4 relatively to its real abundance.

  To calculate the amplification of CH_4 concentration due to the aerosol / albedo difference between the BG and SR, we use a linear fitting between the aerosol / albedo and XCH4 which has the form $y = ax+b$ (see fig. 2.8 below). From the obtained equation, we calculate the DX caused by the mean difference of aerosol / albedo of the two boxes. The error, e is computed from the equation obtained by linear fitting:

$$e = a(x_{SR} - x_{BG})\ \ e \in \{alb_e, aer_e\} \tag{2.10}$$

where e: error due to aerosol/albedo difference between the two boxes; a: slope of the equation obtained by the linear fitting between XCH4 and aerosol/albedo; x_{SR}: mean aerosol/albedo of the source box; x_{BG}: mean aerosol/albedo of the background box.

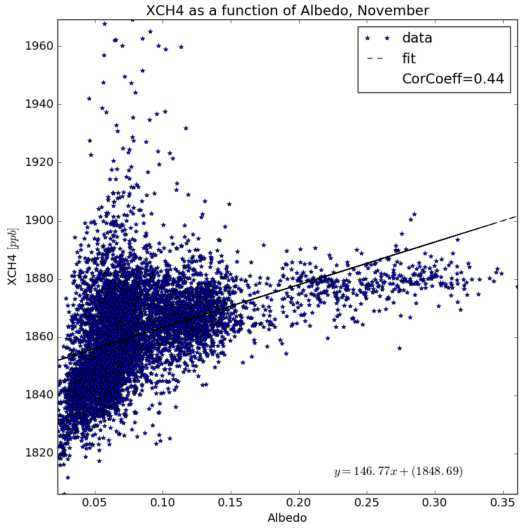

(a)

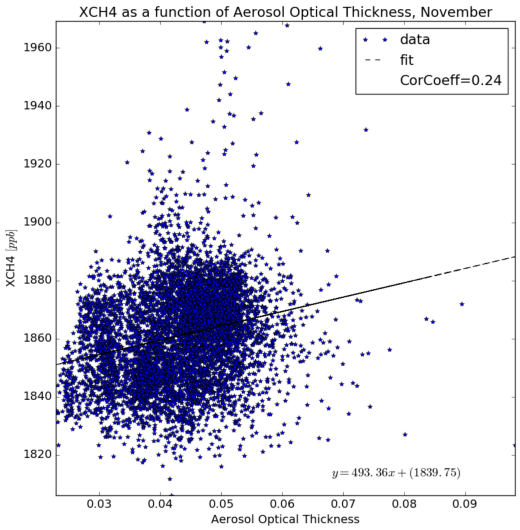

(b)

Figure 2.8: Linear Regression analysis between XCH4 and: a) surface albedo, b) aerosol optical thickness (AOT) for November, 2017.

We compute the total error on DX, σ_{DX} using the following equation:

$$\sigma_{DX} = \sqrt{(pe_{SR})^2 + (pe_{BG})^2 + (alb_e)^2 + (aer_e)^2} \tag{2.11}$$

where σ_{DX}: total DX enhancement error in ppb; pe_{SR}: mean precision error of the source box in ppb; pe_{BG}: mean precision error of the background box in ppb; alb_e: error due to albedo difference between the boxes in ppb; aer_e: error due to aerosol difference between the boxes in ppb.

Similarly, we account for how the error in wind speed and direction propagates to the error on Q.

- **Wind error**: Wind error is taken as 40% of the measurement of wind speed as suggested in Varon et al. [2018].

Finally, we use the following equation to calculate the total error of the source rate Q, σ_Q:

$$\sigma_Q = Q * \sqrt{(\frac{\sigma_{DX}}{DX})^2 + (\frac{\sigma_U}{U})^2} \tag{2.12}$$

where: σ_Q: total error in CH_4 emission rate in tonnes per hour; Q: mean CH_4 emission rate in tonnes per hour; σ_{DX}: total DX enhancement error in ppb, DX means CH_4 enhancement in ppb; σ_U: mean wind error in km per hour; U: mean wind speed in km per hour.

Sensitivity of the method to the wind data

Source Pixel method is sensitive to the wind data as the Q depends linearly on the wind speed as shown in eq. (2.9). For our calculations, we use wind components at $10\ m$ height included in TROPOMI data, which come from European Centre for Medium-Range Weather Forecasts (ECMWF).

In order to validate the selected wind data, we use the high resolution wetland emissions (see fig. 2.5, (b)) as an input tracer to the WRF model. Then, we apply the Source Pixel method to the column averaged CH_4 output of WRF model for the same box and tracer using the wind data from ECMWF. To do so, we use the average of CH_4 concentration, regridded to TROPOMI pixels, for three days, 22, 26 and 27 November, where TROPOMI data over the region is also adequate.

Figure 2.8 shows the result of quantifying emissions Source Pixel method on WRF model output. We find that the result of the model, 61 tonnes of CH_4 per hour, is significantly lower than the emission rate of high resolution wetland emissions, 241 tonnes of CH_4 per hour. The ratio between both emissions gives us a scaling factor S_{wrf}, which can be used to bias correct the Q estimates of the Source Pixel method.

$$S_{wrf} = \frac{Q_{wrf,input}}{Q_{wrf,SPM}} = 3.96 \tag{2.13}$$

The likely reason of the Source Pixel method underestimates is that the average boundary layer wind speed is underestimated using 10 meter wind speeds from ECMWF data. We apply the correction factor S_{wrf} to the initial TROPOMI Q estimates:

$$Q_{TROPOMI,final} = Q_{TROPOMI,initial} * S_{wrf} \tag{2.14}$$

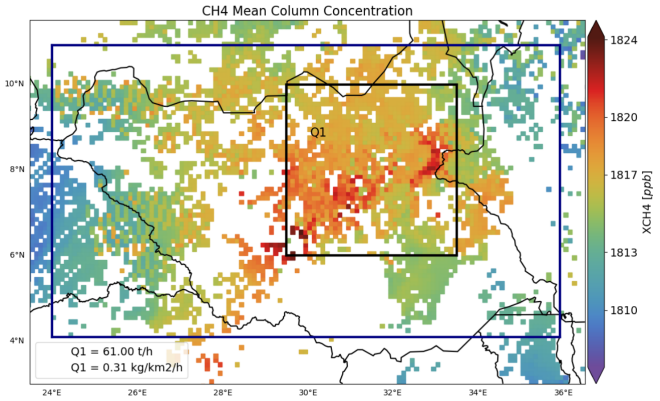

(a)

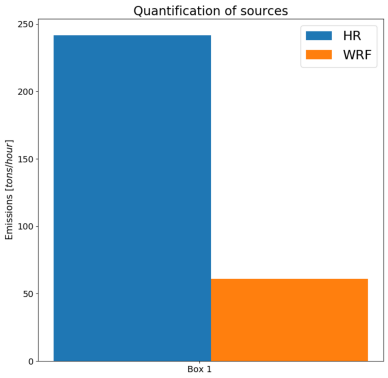

(b)

Figure 2.8: a) Total column CH_4 concentration provided by WRF model after averaging of 3 days (22, 26 and 27 November). **Black square**: source box that includes the wetland area of South Sudan. Blue rectangle: background box used as a reference value for defining the enhancement of XCH4 (source box is excluded), b) CH_4 emission rates computed by high resolution wetland emissions directly (blue bar) and applying Source Pixel method for WRF model data (orange bar).

2.3.3 Other Wetland Models

Finally, we compare the CH_4 emissions estimates with individual sources based on process-based models of CH_4 wetland emissions. We use the following models:

- LPJ and high resolution wetland emissions as explained in section 2.2.2 [Hodson et al., 2011].
- ORCHIDEE wetland emissions and wetland fraction [Ringeval et al., 2010].
- WetCHARTs version 1.0 (extended ensemble) [Bloom et al., 2017].

We compute the mean CH_4 emissions by these models for the TROPOMI source box to compare with our CH_4 emissions estimates.

3 Results and Discussion

In this chapter, we present the main results of this work. We start in section 3.1 introducing the orbitwise TROPOMI CH_4 total column concertation (XCH4) data and, we compare it with the XCH4 data produced by the WRF model. In section 3.2, we show the temporally averaged, and spatially regridded, XCH4 data for November and December, 2017. For these months, we quantify the mean CH_4 emissions caused by wetlands. Furthermore, we compare the wetland emission estimates with several bottom-up models that provide information about wetland CH_4 emissions and wetland fraction.

3.1 Analysing TROPOMI orbital data

3.1.1 Representation of TROPOMI orbital data

As previously explained, section section 2.2.3 , TROPOMI accomplishes a daily overpass over the region of South Sudan due to its wide swath of $2600\ km$. However, the presence of clouds limits the number of orbits with adequate data. During the time period between 13 November and 30 December 2017 only 7 orbits of TROPOMI are considered suitable for study: they contain enough valid data points, 100 pixels per orbit, that are evenly distributed over the region. In this section, we illustrate our orbitwise XCH4 analysis with a focus on the local orbit of 26 November 2017, which is an example of good TROPOMI coverage over the region including South Sudan (between 2° and 11.5°N latitudes and 24° and 36° E longitudes).

Figure 3.1, left graph, displays the TROPOMI XCH4 on 26 November, 2017 (TROPOMI Orbit number 625). We can observe an enhancement of XCH4 at the center of South Sudan. The right graph shows the XCH4_priori (See table 2.2) model for the same day. The XCH4_priori provides the initial value for the TROPOMI XCH4 full-physics retrieval algorithm. It is a global transport model output that takes into consideration information about the topographic variation of the region and adjusts the XCH4 value depending on altitude and pressure differences. As shown in fig. 3.1, the XCH4_priori show significantly

lower variation than TROPOMI XCH4. Hence, we conclude that the large TROPOMI enhancement at the center of South Sudan is not caused by surface altitude variations.

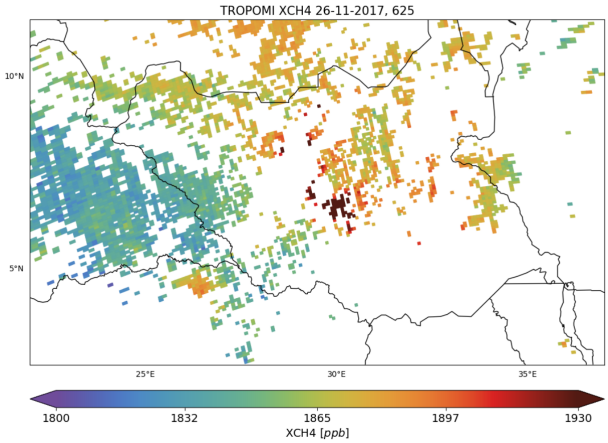

(a)

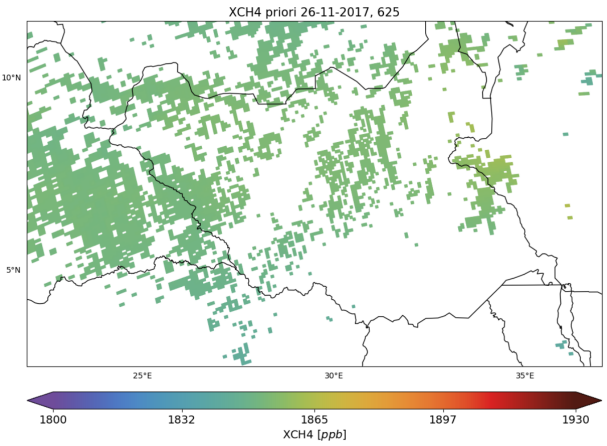

(b)

Figure 3.1: a) TROPOMI XCH4 measurements and b) XCH4_priori for 26 November, 2017 (TROPOMI orbit number 625).

3.1.2 Comparison with WRF model

The total column mean concentration is the sum of WRF-simulated concentration of 6 different tracers: boundaries, EDGAR, high resolution wetland emissions, and 3 separate tracers for emissions from oil and gas activity. The individual contribution of each tracer is shown in fig. 3.2. In fig. 3.3, we present the total column mean concentration of CH_4 (XCH4) produced by the WRF model for the same day that TROPOMI provided adequate data, 26 of November

2017.

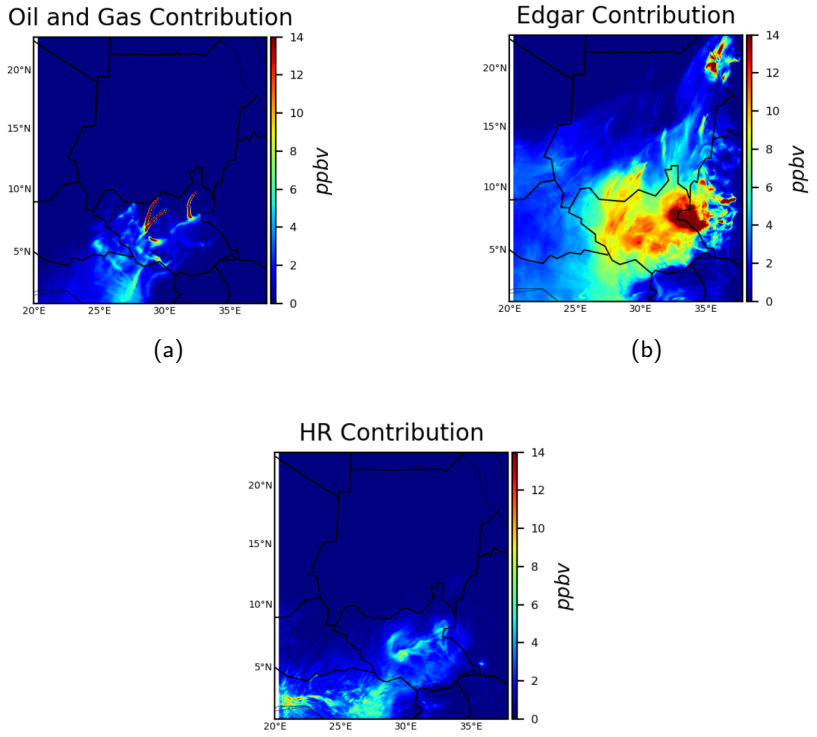

(a) (b)

(c)

Figure 3.2: WRF-simulated total column concentrations of different tracers for 26 November, 2017: a) oil and gas tracers, b) anthropogenic sources (EDGAR), and c) high resolution wetland emissions.

Combining the XCH4 values shown in fig. 3.2 and fig. 3.3, it is clear that the three plumes present in the CH_4 total column concentration are caused by the pixel sources of gas and oil in the northern part of South Sudan. The TROPOMI XCH4 (see fig. 3.1) does not follow the same structure both in XCH4 value and spatial distribution.

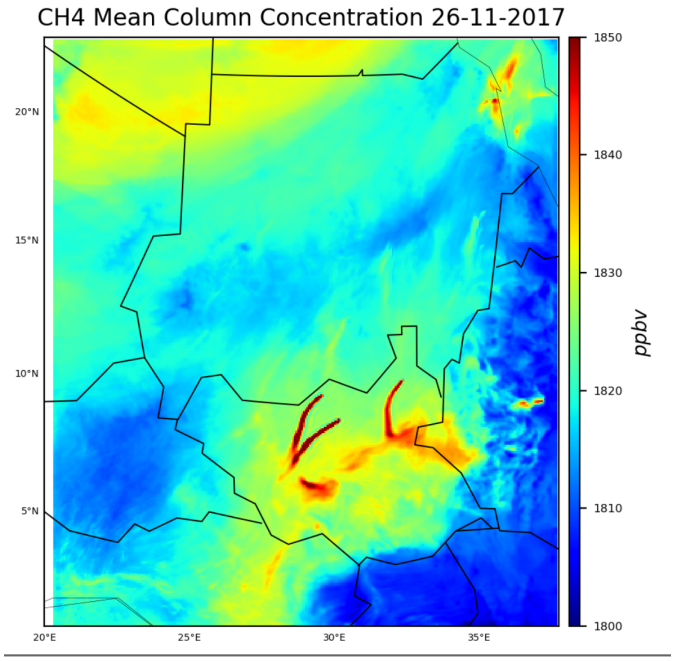

Figure 3.3: Mean total column concentration of CH_4 produced by WRF model for 26 November, 2017, 10:00 UTC-(time that TROPOMI measures over the region).

As we are not interested in the absolute value of CH_4 but rather in its gradient, which is directly influenced by local surface emissions, we show the TROPOMI XCH4 and WRF data after subtracting their respective medians (see fig. 3.4). Moreover, to have a more precise comparison, we exclude from WRF the points where TROPOMI does not have measurements.

In fig. 3.4, we can observe that the pattern of the CH_4 concentration for the two cases partially agrees. However, in the case of the model it is shifted south and eastwards. In addition, the gradient of CH_4 is highly underestimated by the model. The WRF model is incapable of matching the CH_4 spatial distribution of the TROPOMI data.

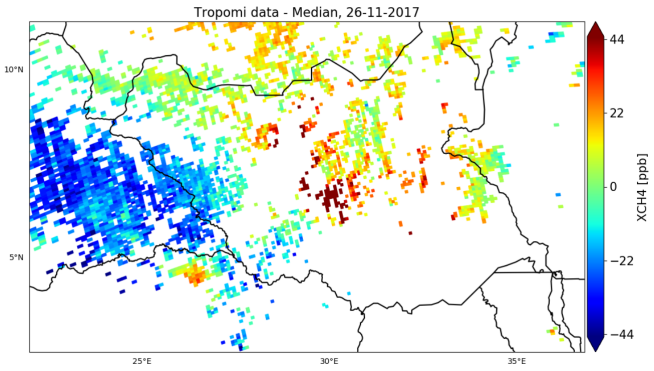

(a)

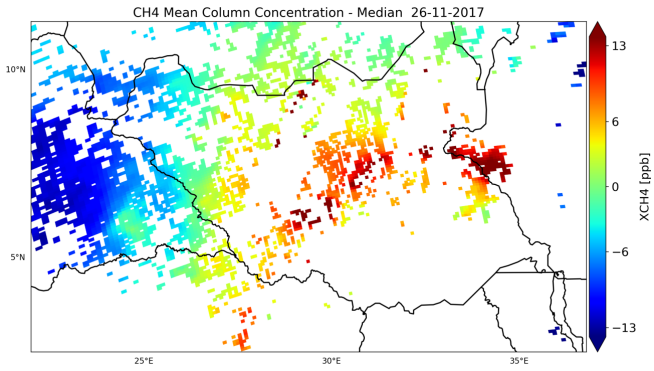

(b)

Figure 3.4: a) TROPOMI and b) WRF XCH4 minus their respective medians. The range of the colorbar is $\pm 2*$standard deviations of XCH4 values in the respective plots.

3.1.3 Optimizing WRF tracers

In order to improve the emission estimates, we minimize the difference between the observations from TROPOMI and the WRF model as explained in section section 2.3.1. Therefore, we define the following cost function J:

$$J = \overline{\sqrt{(XCH4 - (\alpha * Boundary + \beta * Wetlands + \gamma * EDGAR \ldots))^2}} \quad (3.1)$$

The cost function consists of the difference between the observations and each tracer multiplied by its own factor. For each tracer, we initially set its value to 1 which leads to a cost of $43.1\ ppb$; after minimization the cost reduces to $18.3 ppb$. In table 3.1, we present the result of the minimization method with the initial and final values of the cost function. The table also shows the individual scaling factors needed to achieve the minimum value of the cost function.

Figure 3.5 presents the differences between the TROPOMI and the WRF XCH4 before and after the minimization process. We can observe that the initial

Table 3.1: Final scaling factor for each WRF tracer, and values of cost function, derived from the minimization process.

	Scaling Factor
Boundary	1.02
Wetlands	2.02
EDGAR	2.38
Oil and Gas 1	0
Oil and Gas 2	1.09
Oil an Gas 3	0
Cost function	Initially: 43.1
	Finally: 18.3

agreement is not satisfying because the difference has high values all over the region ($J = 43.1\,ppb$). After applying the process, the mismatch between WRF and TROPOMI improves substantially ($J = 18.3\,ppb$). However, the mismatch in the enhancement located in the center of South Sudan does not improve after minimization.

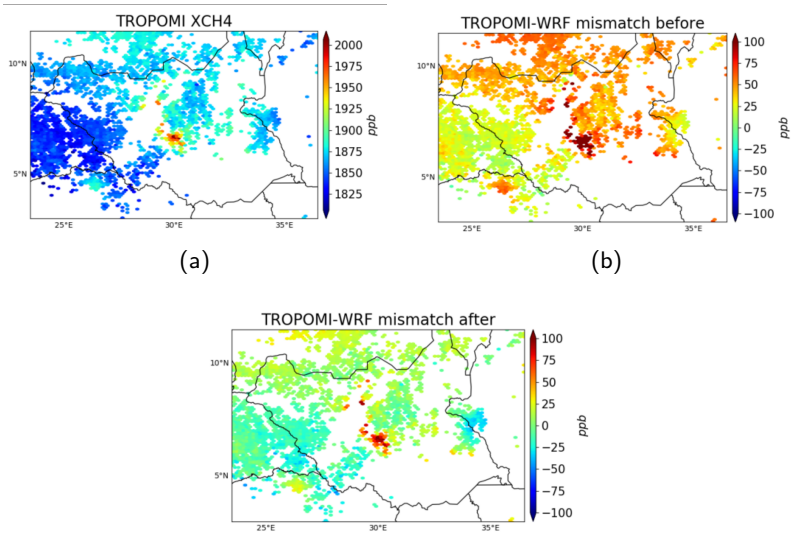

Figure 3.5: a) TROPOMI orbitwise plot of XCH4 for 26 of November, 2017, difference between TROPOMI and WRF XCH4 b) before and c) after the minimization.

The area where the difference has not improved corresponds to the location of the enhancement of XCH4 from TROPOMI. This is likely due to lack of the six WRF tracers to adequately capture the spatial patterns of TROPOMI XCH4.

Moreover, we quantify how much scaling of each individual tracer is needed, if they had to explain the TROPOMI XCH4 values. After regridding WRF to TROPOMI pixels, we calculate the ratio between the average of above 80 percentile XCH4 of TROPOMI and each of the WRF tracers. This process ignores the spatial distributions and assumes that in each case only one tracer is responsible for the enhancement. These ratios between TROPOMI and WRF tracer data is presented in the table 3.2:

Table 3.2: Ratio between the average of above 80 percentile XCH4 of TROPOMI and each of the WRF tracers.

Tracer	**Ratio**
Wetlands	7.74
EDGAR	4.90
Oil and Gas 1	10.39
Oil and Gas 2	8.62
Oil and Gas 3	9.92

Assuming that wetland emissions are only responsible for the XCH4 enhancement seen in TROPOMI data, we have to increase the concentration of CH_4 caused by this tracer approximately 8 times. The linear relation between concentration and emissions in the model implies that the wetland emissions would also be 8 times bigger.

3.1.4 Sensitivity test of WRF

To test whether different microphysics options influence the WRF-simulated XCH4, we do an ensemble of different physical parameterizations of the model before its execution. We modify the microphysics physical parameter which specifies the physical processes that governs the atmospheric heat and moisture tendencies of the model. In order to perform the test, we execute the model eight times, one for each microphysics option and we compute the difference between the maximum and minimum values for each pixel in the map among all different options.

Figure 3.6 illustrates the concentration of CH_4 produced by taking only into account the combination of the three oil and gas sources that represent gas and oil activity. In the top panel, we selected the default microphysics option. In the bottom panel, we show the difference between the maximum and the minimum concentration of CH_4 generated with the different microphysics runs for each tracer of oil and gas activity.

We observe in fig. 3.6 that different microphysics options induce a slight change of the CH_4 gradient. The range of these changes is not enough to explain why the concentration of CH_4 computed by WRF does not match the spatial patterns of XCH4 measured by TROPOMI. In addition, the direction of

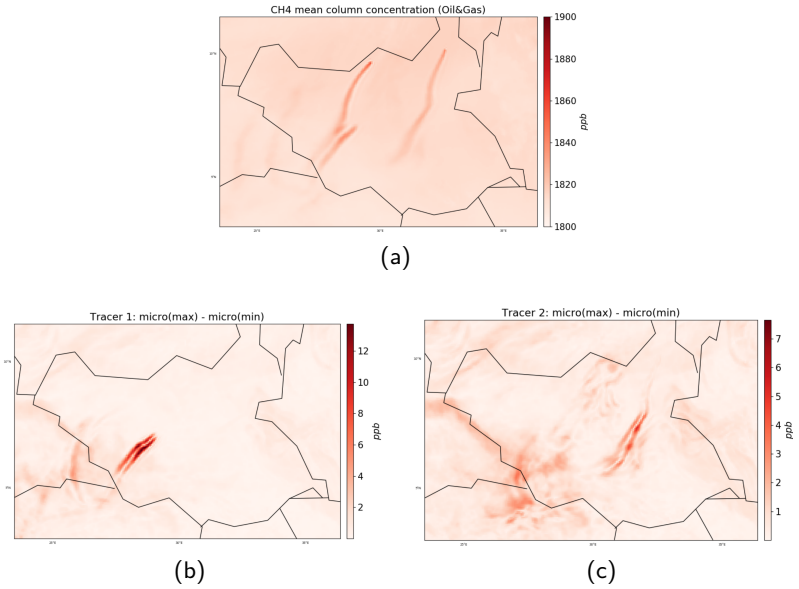

Figure 3.6: a) CH_4 mean column concentration produced by WRF model with oil gas tracers, and b, c) difference between the maximum and the minimum concentration of CH_4 generated with the different microphysics runs for two tracers of oil and gas activity.

the plume is consistent across the microphysics options. We can conclude that the use of an inadequate microphysics options is not the cause of mismatch between the spatial distributions of CH_4.

3.2 TROPOMI monthly averages

3.2.1 Representation of TROPOMI monthly data

In fig. 3.7, we show TROPOMI data regridded to a regular grid of 0.1 degree spatial resolution for November 2017. We can observe that the pattern of XCH4_priori (see fig. 3.7, b) does not show a significant variation over South Sudan, thus the measurements of XCH4 are not affected by surface altitude errors (for more information section 2.1.2 and table 2.2). The monthly mean XCH4, as explained in section 2.1.3, is weighted with the precision value individual pixel measurements. The precision error of the regridded data is shown in fig. 3.7 (d). In fig. 3.8, we present the monthly regridded graphs for December, 2017.

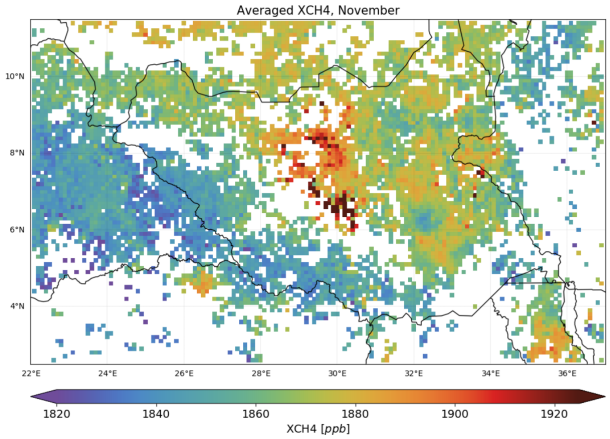
Averaged XCH4, November
10°N
8°N
6°N
4°N
22°E
24°E
26°E
28°E
30°E
32°E
34°E
36°E
1820
1840
1860
1880
1900
1920
XCH4 [ppb]

(a)

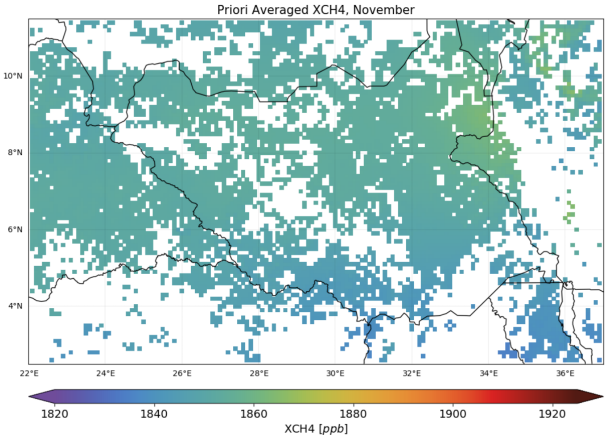
Priori Averaged XCH4, November
10°N
8°N
6°N
4°N
22°E
24°E
26°E
28°E
30°E
32°E
34°E
36°E
1820
1840
1860
1880
1900
1920
XCH4 [ppb]

(b)

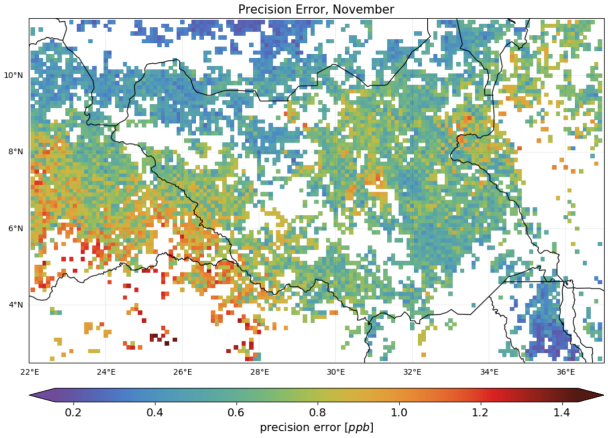
Precision Error, November
10°N
8°N
6°N
4°N
22°E
24°E
26°E
28°E
30°E
32°E
34°E
36°E
0.2
0.4
0.6
0.8
1.0
1.2
1.4
precision error [ppb]

(c)

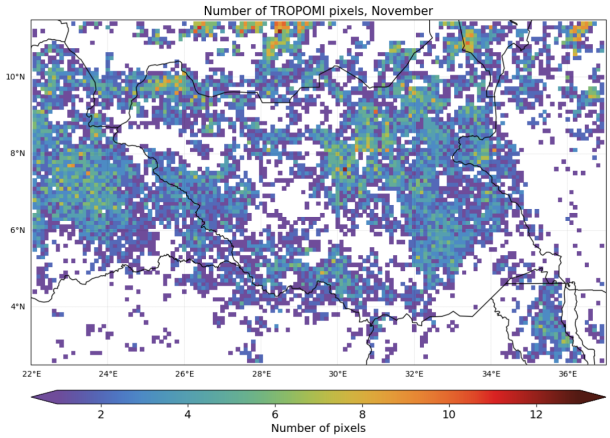

(d)

Figure 3.7: a) Averaged TROPOMI XCH4, b) priori XCH4 and c) precision error regridded to 0.1 degrees spatial resolution, and d) number of TROPOMI pixels contributing to the monthly mean computation for each regular grid cell for November

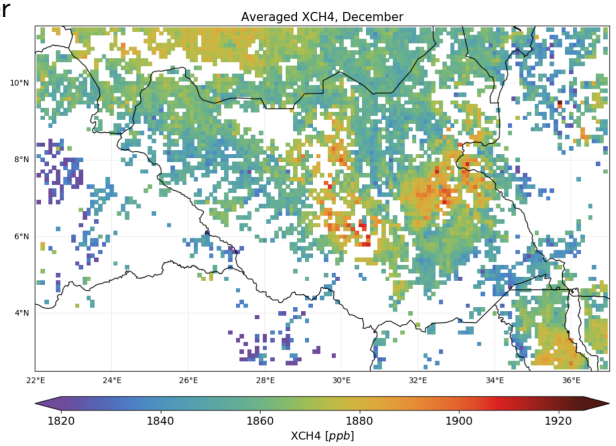

(a)

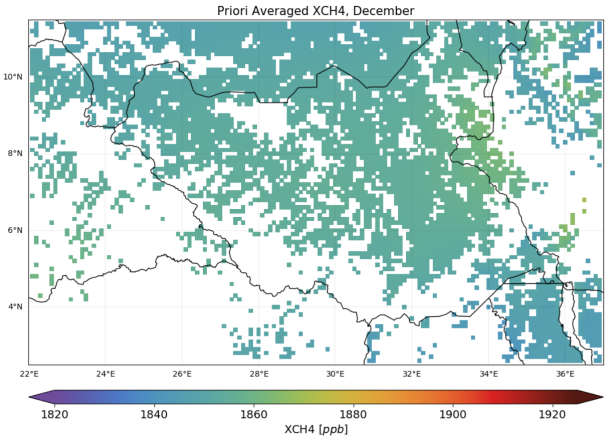

(b)

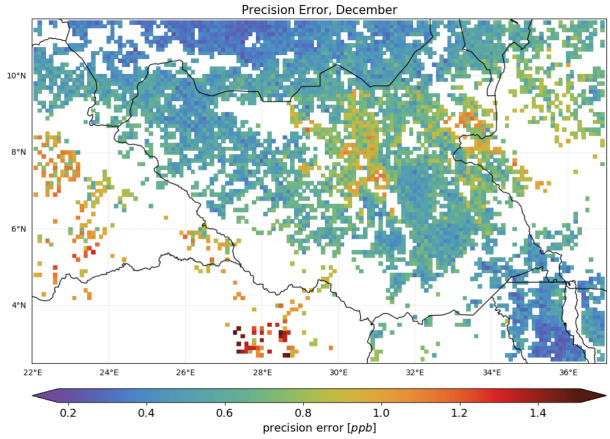

(c)

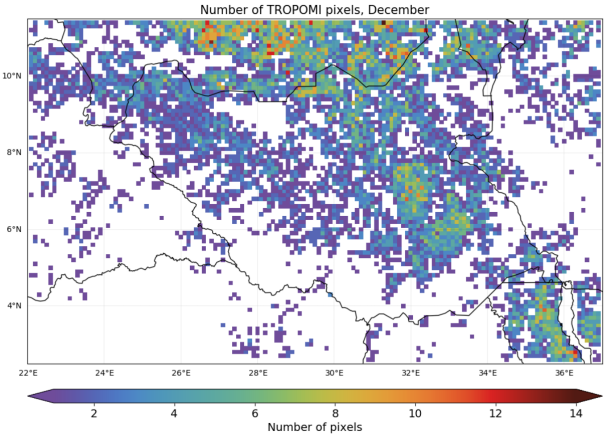

(d)

Figure 3.8: Similar to fig. 3.7 but for December.

Comparing the monthly averaged XCH4 of November and December, we observe that the XCH4 for November shows a higher enhancement over South Sudan. In addition to the concentration of XCH4, the XCH4 enhancement in the center of the country is larger for November. Whereas for December, the enhancement is more spread through the country. Furthermore, the enhancement in both months co-locates with the wetland area of South Sudan (see fig. 2.5 (b)).

Figure 3.9 shows the monthly values of wetland emissions and wetland fraction provided by the LPJ dataset for the year 2014. We can see that both wetland emissions and wetland fraction follow a similar seasonal pattern. However, the seasonal variation of emissions is larger than that of wetland fraction. Moreover, we observe that the wetland emissions decreases by nearly half from November to December.

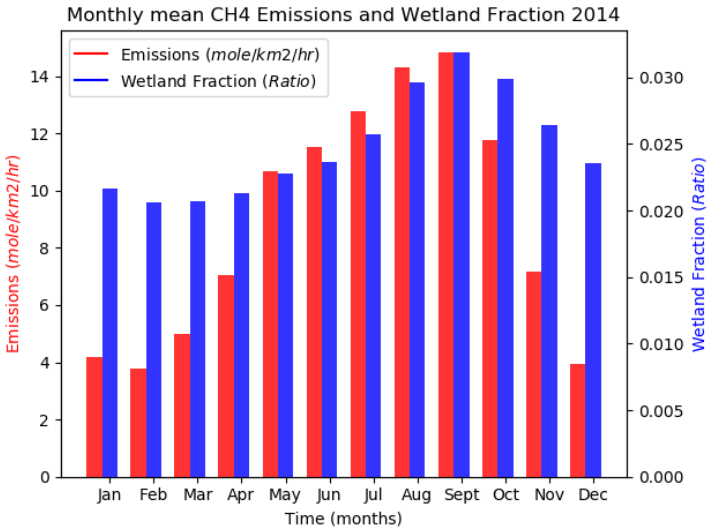

Figure 3.9: Monthly mean wetland emissions (red bar, left x-axis) and wetland fraction (blue bar, right x-axis) for the year 2014 given by LPJ model for the target region

Combining the results from fig. 3.7(a), fig. 3.8(a) and fig. 3.9, we conclude that the seasonal variation of the XCH4 enhancement in observations, agrees with the seasonal pattern suggested by the LPJ model. In contrast, it is unlikely for the anthropogenic emissions to have such a seasonal variation. Therefore, we assume that the wetland emissions are the dominant cause of the XCH4 enhancement measured by TROPOMI over the region of South Sudan.

3.2.2 Emission Quantification from TROPOMI monthly averages

To quantify the CH_4 emission rate of wetlands that are responsible for the observed enhancement of XCH4 in the South Sudan region, we apply the so called Source Pixel method (section 2.3.2). The advantage of this method is that we are not dependent on a transport model output, which can be error prone. Assuming that the enhancement is caused by the wetlands, as inferred in the previous section, we select the source box directly over the region that includes the main wetlands in South Sudan according to the high resolution wetland emissions map (see fig. 2.5).

The estimation of emissions using the Source Pixel method is sensitive to the placement of the background box. In this work, we observed that the shape and location of the background box impacts the calculated CH_4 enhancement, see eq. (2.9). Therefore, for the background box, we select a larger box enclosing the source box. The background region does not include the pixels in the source box since it represents a reference value that is not affected by sources of CH_4 in the source box [Buchwitz et al., 2017], fig. 3.10.

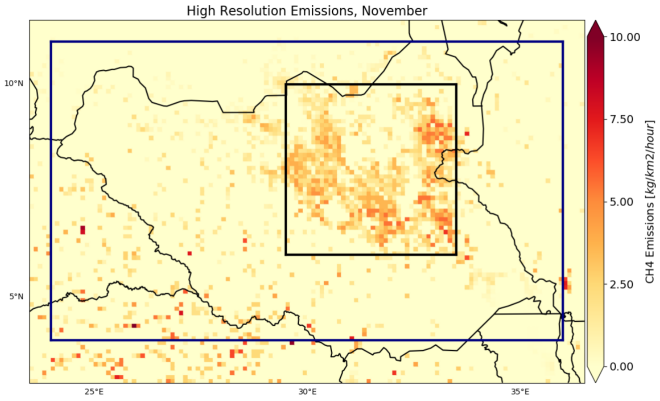

Figure 3.10: High resolution wetland emissions for November. Black square is: source box for quantifying wetland emissions using the Source Pixel method; Blue rectangle is: background box.

Figure 3.11 presents the monthly mean XCH4 for November and December, 2017 in, left and right panels, respectively. The source box and the background box are same as in fig. 3.10. We observe that, consistent with the data obtained from the LPJ model (see fig. 3.9), the CH_4 source rate is higher for November than December, 268 tonnes per hour and 143 tonnes per hour, respectively. Also noticeable in the figure is that, the highest CH_4 concentrations are included within the source box for both months, consistent with our hypothesis that the dominant source of XCH4 enhancement is Wetlands. We do observe high XCH4 values west of the source box, especially for the month of November, which can be due to CH_4 transported by wind.

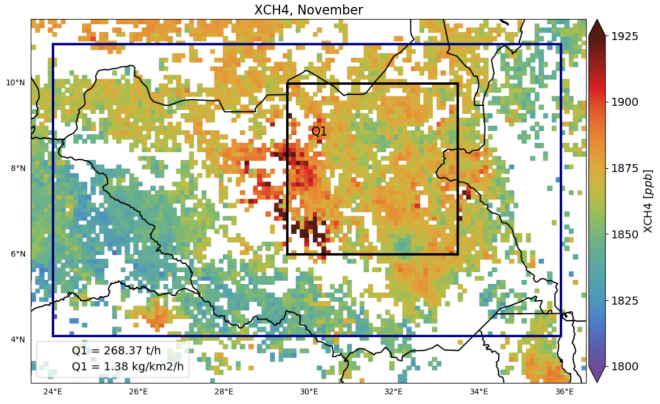

(a)

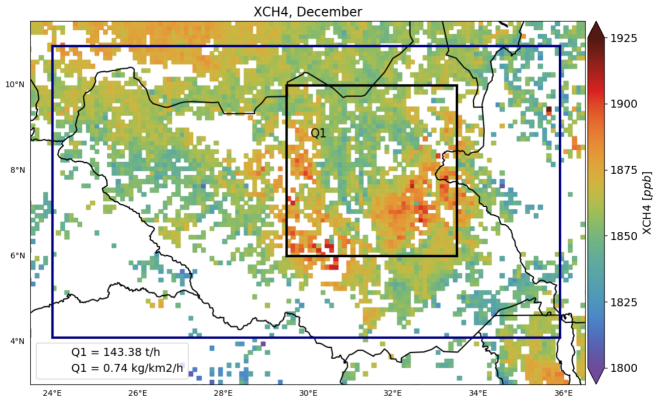

(b)

Figure 3.11: Monthly mean XCH4 for: a) November and b) December. **B**lack square: source box that includes the wetland area of South Sudan (See fig. 3.10). Blue rectangle: background box used as a reference value for defining the enhancement of XCH4 (the source box region is excluded from the background box).

In the table 3.3 we show the parameter used for the source quantification and the respective errors: the mean absolute wind speed of the source box U; the length of side of the source square box W, and the enhancement of XCH4, DX. Other parameters shown are the aerosol optical thickness (AOT) and the surface albedo for the source and the background box.

Table 3.3: Emissions quantification using Source pixel method for November and December, 2017.

	November		December	
Q $[t/h]$	268.37 ± 113.20		143.38 ± 88.74	
U $[km/h]$	9.60 ± 3.84		8.82 ± 3.53	
W $[km]$	441.54		441.54	
ΔX $[ppb]$	11.67 ± 1.59		6.80 ± 3.22	
AOT	0.043	0.043	0.050	0.050
Albedo	0.07	0.08	0.09	0.12

As displayed in table 3.3, the magnitude of the wind speed is the same for both months. The ventilated side of the source box is the same as well, since the box remains the same. The main factor responsible for the reduction of the emission rate, Q, from November to December, is the enhancement, DX, which reduces significantly. Such decrement is consistent with the seasonal pattern suggested by the LPJ model (see fig. 3.9).

As explained in section 2.3.2, it is likely that using 10 meter wind speeds

from ECMWF data in the Source Pixel method, the average boundary layer wind speed is underestimated. The correction factor S_{wrf} applied to the TROPOMI Q estimates is given by the eq. (2.13):

$$Q_{TROPOMI\,final} = Q_{TROPOMI\,initial} * S_{wrf} \tag{3.2}$$

The CH_4 emissions that we obtain after the applying the correction are presented in fig. 3.12.

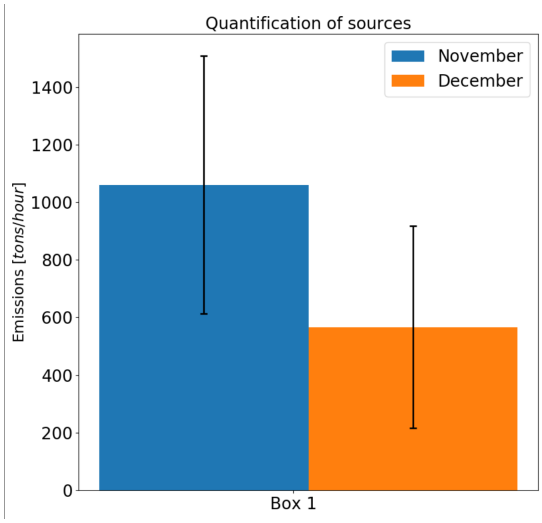

Figure 3.12: TROPOMI CH_4 emission rates after applying the correction factor S_{wrf}.

3.2.3 Comparison with process Models

Figure 3.13 shows the total CH_4 emissions from several process models (see section 2.3.3) for the source box and emission rates computed using TROPOMI data for 2017 (section 2.1.3). The first two groups of bars are for the months of November and December of 2010; the last two bars correspond to the same months but of the most recent year for which the databases are available (for LPJ, *wet_chart_extented* and high resolution it is 2014, while for Orchidee it is 2012). For *wet_chart_extented*, we used the mean of ensemble runs provided in the dataset and the maximum emissions.

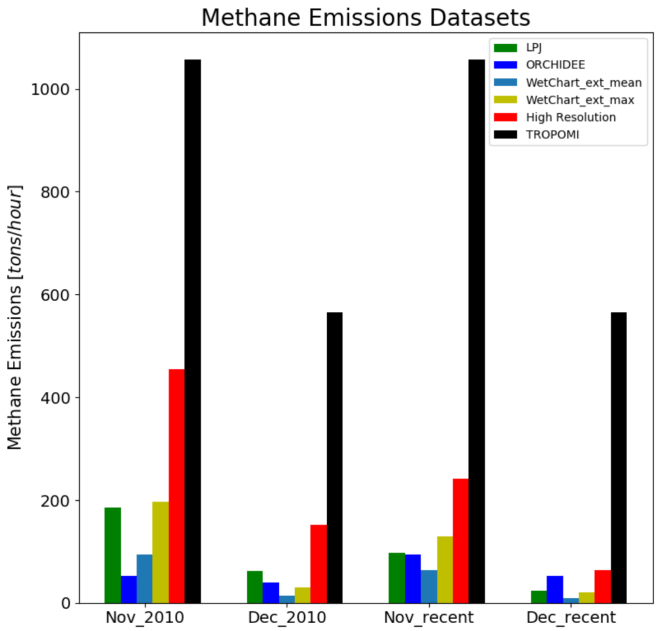

Figure 3.13: Total CH_4 emissions from wetland process models and computed TROPOMI emission rates for November and December 2017.

From fig. 3.13, we observe that all the model inventories highly underestimate the CH_4 emissions produced by wetlands in comparison to the TROPOMI estimates. The high resolution model, explained in section 2.2.2 is the one that results in higher values of CH_4 concentrations although it still greatly differs from the observation.

Figure 3.14 presents the mean wetland fraction of the source box as provided by LPJ, Orchidee and the high resolution wetlands dataset. In this case, the first bar groups also show the mean wetland fraction for November and December of 2010, while the second bar group corresponds to the year 2014 for LPJ and high resolution wetland dataset , and to 2012 for the Orchidee model. We find that the wetland fraction is greatly underestimated in all the process models in comparison to the high resolution dataset's wetland fractions. This might be due to the fact that the HR model is at a finer resolution of 231 m and hence resolves the wetlands fractions better than the coarse resolution ($0.1 \times 0.1\, degrees$ or $\sim 50 \times 50\, km^2$) wetlands models.

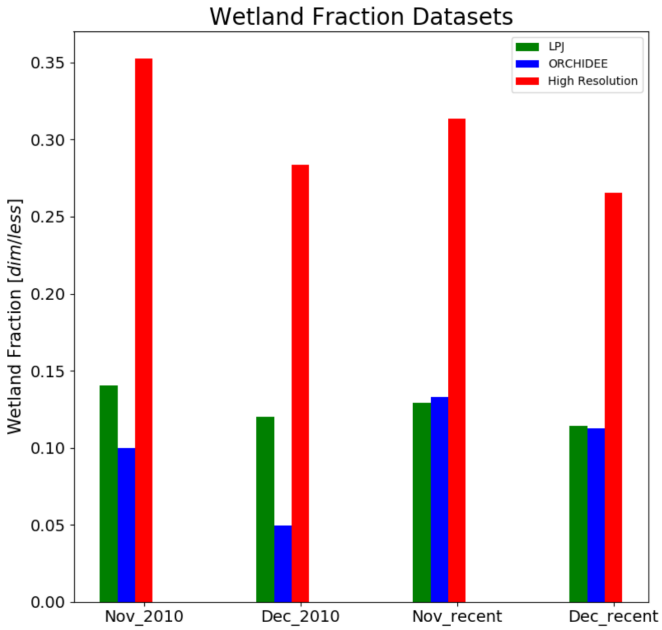

Figure 3.14: Mean wetland fraction from wetland process models.

4 Conclusions

The primary objective of this study was to estimate CH_4 emissions in the region of South Sudan, which allowed us to understand the unexpectedly high concentration of CH_4 measured by TROPOMI. In order to do so, we used multiple emission quantification methods. First, we compared the CH_4 mixing ratios retrieved by TROPOMI and those computed from the atmospheric transport model WRF; Second, we used the model-independent Source Pixel method. Finally, we compared the CH_4 emissions from multiple process-based models with the emissions calculated from TROPOMI data.

The WRF model shows difficulties following the spatial distribution of XCH4 enhancements of TROPOMI. By comparing the WRF simulated CH_4 concentration with the orbital TROPOMI XCH4, we found that the gradient of XCH4 is underestimated by the model. The main reason is that the emissions taken as an input to the model are too low. By minimizing the difference between the observations (TROPOMI) and the model (WRF), we found that for a better agreement, the WRF emissions needed to be scaled up by a factor of approximately 8 for the anthropogenic and wetland emissions.

In order to study in further detail, we calculated monthly averaged TROPOMI XCH4 data for November and December 2017, as the monthly averages of XCH4 are more robust against CH_4 variation caused by short term meteorological conditions. We observed that the TROPOMI XCH4 enhancement for these months follows the pattern of high resolution wetland map. In addition, the enhancement follows the seasonality pattern suggested by the CH_4 emissions from the LPJ wetlands model. Therefore, we conclude that it is likely that the main source of CH_4 in South Sudan is wetlands since anthropogenic activities cannot explain the observed spatiotemporal patterns.

Within the scope of this work, we confirmed that TROPOMI allows us to detect and localize sources of CH_4 with high accuracy and precision. By applying the Source Pixel method for the months of November and December 2017, we were able to quantify emissions of CH_4 in the region of interest. We obtained an emission rate of $1057. \pm 447$ tonnes of CH_4 per hour for November and 566 ± 348 tonnes CH_4 per hour for December.

We used the result of TROPOMI source rate estimation to validate existing CH_4 emissions of wetland models. These inventories follow the trend suggested by TROPOMI measurements; however, they highly underestimate the actual values of the wetland emissions in South Sudan. Comparing the high resolution wetland fraction dataset and the wetland fraction used in the models, we found that the latter is also highly underestimated. Because there is a strong correlation between wetland emissions and wetland fraction (correlation coefficient $= 0.83$), as shown by the LPJ model, it is likely that the cause of underestimation of wetland emissions in the models is the underestimation of wetland fraction.

4.1 Future work

Since TROPOMI has been recently launched on 13 October, 2017, the available data is only for a short time period. An interesting prospect would be to apply the emissions estimation methods used in this study on data from a longer time period to investigate on greater detail the CH_4 wetland emissions seasonal pattern over the region of South Sudan.

As explained in this study, the Source Pixel method is very sensitive to the selection of wind data. Therefore, a next step could be to validate the wind model data with local wind measurements in the region to select the most accurate model in order to reduce the error induced by wind in the source quantification. In addition, other methods for estimating CH4 emissions can be applied when the situation allows: Gaussian Plume inversion [Fioletov et al., 2015] or Cross-sectional Flux method [Krings et al., 2011, 2013] when the location of the source is known; Integrated Mass Enhancement (IME) [Frankenberg et al., 2016] when the exact position of the source is not known.

By estimating the CH_4 emissions using TROPOMI data, we could validate the process-based wetland model. Using this information, one could improve the input dataset to the WRF model and improve the WRF simulations. In this work, we ran the model with different microphysics options although as discussed this did not explain the mismatch between TROPOMI and WRF XCH4. Another way to test the accuracy of the WRF model is to try various other combinations of physical parameters such as the planetary boundary layer schemes.

Bibliography

Understanding global warming potentials. https://www.epa.gov/ghgemissions/understanding-global-warming-potentials. Accessed: 2018-11-21.

Satellites improve air quality monitoring in south africa. http://www.esa.int/Our_Activities/Observing_the_Earth/Satellites_improve_air_quality_monitoring_in_South_Africa. Accessed: 2018-11-23.

A. A. Bloom, K. W. Bowman, M. Lee, A. J. Turner, R. Schroeder, J. R. Worden, R. Weidner, K. C. McDonald, and D. J. Jacob. A global wetland methane emissions and uncertainty dataset for atmospheric chemical transport models (wetcharts version 1.0). *Geoscientific Model Development*, 10(6):2141–2156, 2017.

T. Borsdorff, J. Aan de Brugh, H. Hu, I. Aben, O. Hasekamp, and J. Landgraf. Measuring carbon monoxide with tropomi: First results and a comparison with ecmwf-ifs analysis data. *Geophysical Research Letters*, 45(6):2826–2832. doi: 10.1002/2018GL077045. URL https://agupubs.onlinelibrary.wiley.com/doi/abs/10.1002/2018GL077045.

T. Borsdorff, J. aan de Brugh, S. Pandey, O. Hasekamp, I. Aben, S. Houweling, and J. Landgraf. Carbon monoxide air-pollution on sub-city scales and along arterial roads detected by the tropospheric monitoring instrument. *Atmospheric Chemistry and Physics Discussions*, 2018:1–17, 2018. doi: 10.5194/acp-2018-1185. URL https://www.atmos-chem-phys-discuss.net/acp-2018-1185/.

M. Buchwitz, O. Schneising, M. Reuter, J. Heymann, S. Krautwurst, H. Bovensmann, J. P. Burrows, H. Boesch, R. J. Parker, P. Somkuti, et al. Satellite-derived methane hotspot emission estimates using a fast data-driven method. 2017.

A. Butz, O. P. Hasekamp, C. Frankenberg, and I. Aben. Retrievals of atmospheric co 2 from simulated space-borne measurements of backscattered near-infrared sunlight: Accounting for aerosol effects. *Applied optics*, 48(18): 3322–3336, 2009.

A. Butz, S. Guerlet, O. Hasekamp, D. Schepers, A. Galli, I. Aben, C. Frankenberg, J.-M. Hartmann, H. Tran, A. Kuze, et al. Toward accurate co2 and ch4 observations from gosat. *Geophysical Research Letters*, 38(14), 2011.

P. Ciais, C. Sabine, G. Bala, L. Bopp, V. Brovkin, J. Canadell, A. Chhabra, R. DeFries, J. Galloway, M. Heimann, et al. Carbon and other biogeochemical cycles. In *Climate change 2013: the physical science basis. Contribution of Working Group I to the Fifth Assessment Report of the Intergovernmental Panel on Climate Change*, pages 465–570. Cambridge University Press, 2014.

M. Crippa, D. Guizzardi, M. Muntean, E. Schaaf, F. Dentener, J. A. van Aardenne, S. Monni, U. Doering, J. G. Olivier, V. Pagliari, et al. Gridded emissions of air pollutants for the period 1970-2012 within edgar v4. 3.2. *Earth System Science Data*, 10:1987–2013, 2018.

E. J. Dlugokencky, E. G. Nisbet, R. Fisher, and D. Lowry. Global atmospheric methane: budget, changes and dangers. *Philosophical Transactions of the Royal Society of London A: Mathematical, Physical and Engineering Sciences*, 369(1943):2058–2072, 2011.

V. E. Fioletov, C. A. McLinden, N. Krotkov, and C. Li. Lifetimes and emissions of so2 from point sources estimated from omi. *Geophysical Research Letters*, 42(6):1969–1976, 2015. doi: 10.1002/2015GL063148. URL `https://agupubs.onlinelibrary.wiley.com/doi/abs/10.1002/2015GL063148`.

C. Frankenberg, I. Aben, P. Bergamaschi, E. Dlugokencky, R. Van Hees, S. Houweling, P. Van Der Meer, R. Snel, and P. Tol. Global column-averaged methane mixing ratios from 2003 to 2009 as derived from sciamachy: Trends and variability. *Journal of Geophysical Research: Atmospheres*, 116(D4), 2011.

C. Frankenberg, A. K. Thorpe, D. R. Thompson, G. Hulley, E. A. Kort, N. Vance, J. Borchardt, T. Krings, K. Gerilowski, C. Sweeney, et al. Airborne methane remote measurements reveal heavy-tail flux distribution in four corners region. *Proceedings of the National Academy of Sciences*, 113(35):9734–9739, 2016.

G. A. Grell, S. E. Peckham, R. Schmitz, S. A. McKeen, G. Frost, W. C. Skamarock, and B. Eder. Fully coupled "online" chemistry within the wrf model. *Atmospheric Environment*, 39(37):6957–6975, 2005.

T. Gumbricht, R. Román-Cuesta, L. Verchot, M. Herold, F. Wittmann, E. Householder, N. Herold, and D. Murdiyarso. Tropical and subtropical

wetlands distribution version 2, 2018. URL https://doi.org/10.17528/CIFOR/DATA.00058.

O. P. Hasekamp and A. Butz. Efficient calculation of intensity and polarization spectra in vertically inhomogeneous scattering and absorbing atmospheres. *Journal of Geophysical Research: Atmospheres*, 113(D20), 2008.

E. Hodson, B. Poulter, N. Zimmermann, C. Prigent, and J. O. Kaplan. The el niño–southern oscillation and wetland methane interannual variability. *Geophysical Research Letters*, 38(8), 2011.

S. Houweling, M. Krol, P. Bergamaschi, C. Frankenberg, E. Dlugokencky, I. Morino, J. Notholt, V. Sherlock, D. Wunch, V. Beck, et al. A multi-year methane inversion using sciamachy, accounting for systematic errors using tccon measurements. *Atmospheric chemistry and physics*, 14(8):3991–4012, 2014.

H. Hu, O. Hasekamp, A. Butz, A. Galli, and J. Landgraf. Aan de brugh. *J., Borsdorff, T., Scheepmaker, R., and Aben, I.: The operational methane retrieval algorithm for TROPOMI, Atmos. Meas. Tech*, 9:5423–5440, 2016.

H. Hu, J. Landgraf, R. Detmers, T. Borsdorff, J. Aan de Brugh, I. Aben, A. Butz, and O. Hasekamp. Toward global mapping of methane with tropomi: first results and intersatellite comparison to gosat. *Geophysical Research Letters*, 45(8):3682–3689, 2018.

D. Jacob. *Introduction to atmospheric chemistry*. Princeton University Press, 1999.

D. J. Jacob, A. J. Turner, J. D. Maasakkers, J. Sheng, K. Sun, X. Liu, K. Chance, I. Aben, J. McKeever, and C. Frankenberg. Satellite observations of atmospheric methane and their value for quantifying methane emissions. *Atmospheric Chemistry and Physics*, 16(22):14371–14396, 2016.

M. Z. Jacobson. Correction to "control of fossil-fuel particulate black carbon and organic matter, possibly the most effective method of slowing global warming". *Journal of Geophysical Research: Atmospheres*, 110(D14). doi: 10.1029/2005JD005888. URL https://agupubs.onlinelibrary.wiley.com/doi/abs/10.1029/2005JD005888.

T. Krings, K. Gerilowski, M. Buchwitz, M. Reuter, A. Tretner, J. Erzinger, D. Heinze, U. Pflüger, J. Burrows, and H. Bovensmann. Mamap–a new spectrometer system for column-averaged methane and carbon dioxide observations from aircraft: Retrieval algorithm and first inversions for point source emission rates. *Atmospheric Measurement Techniques*, 4(9):1735–1758, 2011.

T. Krings, K. Gerilowski, M. Buchwitz, J. Hartmann, T. Sachs, J. Erzinger, J. Burrows, and H. Bovensmann. Quantification of methane emission rates from coal mine ventilation shafts using airborne remote sensing data. *Atmospheric Measurement Techniques*, 6:151–166, 2013.

D. Nijkerk, B. Van Venrooy, P. Van Doorn, F. Draaisma, and A. Hoogstrate. The tropomi telescope, design, fabrication and test of a freeform optical system. In *International Conference on Space Optics ICSO*, 2012.

M. J. Prather, C. D. Holmes, and J. Hsu. Reactive greenhouse gas scenarios: Systematic exploration of uncertainties and the role of atmospheric chemistry. *Geophysical Research Letters*, 39(9), 2012.

B. Ringeval, N. de Noblet-Ducoudré, P. Ciais, P. Bousquet, C. Prigent, F. Papa, and W. B. Rossow. An attempt to quantify the impact of changes in wetland extent on methane emissions on the seasonal and interannual time scales. *Global Biogeochemical Cycles*, 24(2), 2010.

M. Saunois, P. Bousquet, B. Poulter, A. Peregon, P. Ciais, J. G. Canadell, E. J. Dlugokencky, G. Etiope, D. Bastviken, S. Houweling, et al. The global methane budget 2000–2012. *Earth System Science Data (Online)*, 8(2), 2016.

W. Skamarock, J. Klemp, J. Dudhia, D. Gill, D. Barker, W. Wang, and J. Powers. A description of the advanced research wrf version 3. 27:3–27, 01 2008.

T. Stocker, D. Qin, G. Plattner, M. Tignor, S. Allen, J. Boschung, A. Nauels, Y. Xia, V. Bex, and P. Midgley. Ipcc, 2013: Climate change 2013: The physical science basis. contribution of working group i to the fifth assessment report of the intergovernmental panel on climate change, 1535 pp, 2013.

M. van Weele, P. Levelt, I. Aben, P. Veefkind, M. Dobber, H. Eskes, S. Houweling, J. Landgraf, and R. Noordhoek. Science requirements document for tropomi, 2008.

D. J. Varon, D. J. Jacob, J. McKeever, D. Jervis, B. O. Durak, Y. Xia, and Y. Huang. Quantifying methane point sources from fine-scale (ghgsat) satellite observations of atmospheric methane plumes. *Atmospheric Measurement Techniques Discussions*, pages 1–25, 2018.

J. Veefkind, I. Aben, K. McMullan, H. Förster, J. De Vries, G. Otter, J. Claas, H. Eskes, J. De Haan, Q. Kleipool, et al. Tropomi on the esa sentinel-5 precursor: A gmes mission for global observations of the atmospheric composition for climate, air quality and ozone layer applications. *Remote Sensing of Environment*, 120:70–83, 2012.